

R&D 2885-AN

ENGINEERING MODELS OF BALLISTIC
PERFORATION AT HIGH VELOCITIES

AD A128753

Final Technical Report

by

S. R. Bodner

April 1983

United States Army

RESEARCH & STANDARDIZATION GROUP (EUROPE)

London England

CONTRACT NUMBER DAJA37-81-C-0047

Technion Research and Development Foundation

Haifa Israel

DTIC
ELECTE
MAY 31 1983
S D E

DTIC FILE COPY

Approved for Public Release: distribution unlimited

Reproduced From
Best Available Copy

83 05 31 088

REPORT DOCUMENTATION PAGE		READ INSTRUCTIONS BEFORE COMPLETING FORM
1. Report Number	2. Govt Accession No.	3. Recipient's Catalog Number
4. Title (and Subtitle) ENGINEERING MODELS OF BALLISTIC PERFORATION AT HIGH VELOCITIES		5. Type of Report & Period Covered Final Technical Report Oct. 1980 - April 1983
		6. Performing Org. Report Number
7. Author(s) S. R. Bodner		8. Contract or Grant Number DAJA37-81-C-0047
9. Performing Organization Name and Address Technion Research & Development Foundation Haifa 32000, Israel		10. Program Element, Project, Task Area & Work Unit Numbers
11. Controlling Office Name and Address U.S. Army Contracting Agency, Europe Attn: AEUPC-PC, Eschersheimer Landstrasse 163 6000 Frankfurt/Main, GERMANY		12. Report Date April 1983
		13. Number of Pages 66
14. Monitoring Agency Name and Address European Research Office, U.S. Army 223 Old Marylebone Road London, NW1 5TH, ENGLAND		15. Unclassified
16. & 17. Distribution Statement Approved for public release; distribution unlimited.		
18. Supplementary Notes		
19. Key Words Ballistics, Terminal; Impact; Penetration; Perforation; Hopkinson-bar.		
20. Abstract The research program consisted of two main parts: (1) a series of ballistic tests with long rod penetrators of SAE 4140 steel impacting target plates of RHA steel and 5083 aluminum alloy, and (2) the development of an improved five stage engineering model of the ballistic perforation process. In addition, a split-Hopkinson bar (Kolsky bar) arrangement was set up to measure material strength at high rates of loading. Results of the present ballistic tests will be used in conjunction with subsequent improvement of the engineering model to account for projectile mass loss effects. The current model does demonstrate good correlation with ballistic test results in the standard velocity range.		

FORM 1473

Abstract

The research program consisted of two main parts: (1) a series of ballistic tests with long rod penetrators of SAE 4140 steel impacting target plates of RHA steel and 5083 aluminum alloy, and (2) the development of an improved five stage engineering model of the ballistic perforation process. In addition, a split-Hopkinson (Kolsky bar) arrangement was set up to measure material strength at high rates of loading. Results of the present ballistic tests will be used in conjunction with subsequent improvement of the engineering model to account for projectile mass loss effects. The current model does demonstrate good correlation with ballistic test results in the standard velocity range.

Accession For	
NTIS GFA&I	<input checked="" type="checkbox"/>
DTIC TAB	<input type="checkbox"/>
Unannounced	<input type="checkbox"/>
Justification	<input type="checkbox"/>
By	
Distribution/	
Availability Codes	
Avail and/or	
Dist	Special
A	



Description of Research Program

The overall research program consisted of two major parts and a secondary supporting project. The first major task was the design and performance of a series of ballistic tests with long rod penetrators made of SAE 4140 steel. These were used to impact target plates of rolled homogeneous armor steel (RHA) and 5083 H-115 aluminum alloy. Thicknesses of the RHA plates were 75.0 mm and 50.8 mm and the aluminum target consisted of 3 plates in contact, each of 44.5 mm, for a total thickness of 133.5 mm. Impact was normal to the plate with impact velocities ranging from 1356 to 1560 m/s. Eight of the shots were successful in supplying useful information.

The tests were conducted in a well instrumented ballistic range which provided pre-impact velocity measurements by photo-cells and X-ray photographs of the projectile immediately prior and after perforation by flash radiographic equipment. After completion of the ballistic tests, the target plates were sectioned and etched around the perforation cavities which were then subjected to close inspection. Mechanical property tests were also made on the projectile and target materials. Since the perforation process occurs at very high rates of loading, mechanical properties at those rates would be useful in the analytical modelling. This data can be obtained by means of a split Hopkinson pressure bar (Kolsky bar).

When the measured residual velocities following perforation are extrapolated to zero by an analytical procedure, an estimate could be obtained for the ballistic limit velocity, V_L , for the projectile and the various target plates. For the steel plates, V_L for the 75.0 mm

thickness was obtained to be 1325 m/s, while that of the 50.8 mm steel target plate was $V_L = 1150$ m/s. In the case of the aluminum targets, the test data was not sufficient for a reasonable estimate of V_L .

Some of the more important results of the various tests and examinations are attached to this report as Appendix A. The attached figures and tables consist of the following:

- Fig. 1 - Geometry of projectile of SAE 4140 steel.
- Table I - Penetrator: Material composition.
- Table II - Penetrator: Mechanical properties.
- Table III - Target plates: Mechanical properties.
- Table IV - Projectile velocity characteristics prior to impact.
- Table V - Contact time, residual velocity, and physical and geometrical characteristics after perforation.
- Table VI - Dimensions of projectile entrance and exit holes in the target plates.
- Figs. 2,3 - Cavity profiles in steel target plates showing hardness (R_C) measurements.
- Fig. 4 - Cavity profile in an aluminum target.
- Fig. 5 - Hole profile after perforation of 50.8 mm RHA target.
- Fig. 6 - Hole profile after perforation of 75 mm RHA target.
- Fig. 7 - Hole profile after perforation of 133.5 mm AL 5083 H-115 target.
- Fig. 8 - Hole profile after perforation of 133.5 mm AL 5083 H-115 target.
- Fig. 9 - Characterization of the final deformation and hole dimension for Table VII.
- Table VII - Characteristic parameters measured for defining the final target deformation.

This examination of the results of the ballistic tests is intended to serve as a physical basis and motivation for the development of an engineering model of the perforation process at high impact velocities. The test results, especially the residual velocities and residual projectile lengths, will also serve as reference data for

subsequent comparison with analytical predictions. The model would include the effects of erosion of the projectile and of plastic deformation and inertia of the projectile and target.

The second major task was the development of a new five stage engineering model of perforation of a metal target by a rigid projectile of standard ordnance velocities. The initial stage relies on an assumed velocity field for a plastically deforming medium with a moving boundary (the indenter), where the unknown parameters are determined from the upper bound theorem of plasticity modified to include dynamic effects. Subsequent deformation stages include the development of a bulge at the rear surface of the target, the extension of the bulge, the development of a plug and a shear zone, and the ejection of the projectile and plug following material failure. This model is an improvement over that of Averbuch and Bodner as it does not rely on any empirical factors and is more suitable for extension to the case of projectile erosion. A paper describing this model has been prepared, "Dynamic Perforation of Viscoplastic Plates by Rigid Projectiles", by Ravid and Bodner, and appears as Appendix B of this report. It has been accepted for publication in the International Journal of Engineering Science (for publication in 1983). Further improvement of the model to include the effects of projectile mass loss will lead to a theory that could be correlated with the results of the test program.

The secondary supporting project was the setting up of a split-Hopkinson bar arrangement (Kolsky bar) in order to obtain stress-strain relations at high rates of loading. The experimental facility

is shown schematically in Fig. 1. A 12.7 ϕ mm diameter steel projectile embedded in a teflon collar is propelled in a smooth bore (18 ϕ mm) powder gun and strikes the input bar which is made of the same material as the projectile (PH - 15-5). Both input and output bars are identical, each 12.7 ϕ mm in diameter and 876 mm long. The length of the projectile in the present tests was 100 mm and its impact velocity was in the range of 15 to 35 meters per second. The maximum stress produced by the higher velocity was about 720 MPa, which was a little over half the yield stress of the Hopkinson bars. Such low velocities were obtained by shortening the cartridges and using between 0.5 and 1.0 grams of gun powder. The specimens were short disks, 12 mm in diameter with aspect ratios (l/d) of 0.3 to 0.5. The strain pulses were detected by two pairs of strain gauges (WK-06-125AD-350 by Micro Measurement) and recorded by a two channel digital oscilloscope (Explorer 204 by Nicolet).

Four metals and four polymers were each tested at two or three impact velocities and the tests were repeated at least three times. The materials tested were:

- (1) SAE 1070 Steel
- (2) 2011-T3 Aluminum
- (3) 99.93% Purity Electrolytic Copper
- (4) Commercial Brass
- (5) Polyamid (Akulon) 6
- (6) Polytetrafluoroethylene (Teflon)
- (7) Structural adhesive FM-300K
- (8) Structural adhesive FM-73

The oscilloscope records of the tests conducted with the non metallic specimens showed that the reflected pulses were large compared to the transmitted ones, and since the strain rate is approximately proportional to the magnitude of the reflected pulse, this means that the strain rates

in the tests of the non metallic specimens were higher than in the metallic specimens (where the reflected pulses were relatively smaller). It was also clear from the oscilloscope records that the strain rates were not constant throughout the tests but varied in time. In the tests of the non metallic materials one could relate to average values of strain rates, whereas in the tests of the metallic specimens average values were meaningful only over small portions of the loading pulses.

Some of the stress-strain curves are shown in Figs.2-5. The curves of the non metallic specimens are given with indications of the average strain rates for each curve, whereas the results of the metallic specimens are presented with indications of the maximum values of the strain rates.

The personnel who worked on the research program during this period are: Professor S. R. Bodner, Associate Professor J. M. Lifshitz, and Mr. Moshe Ravid and Mr. Ezra Scher, both graduate students.

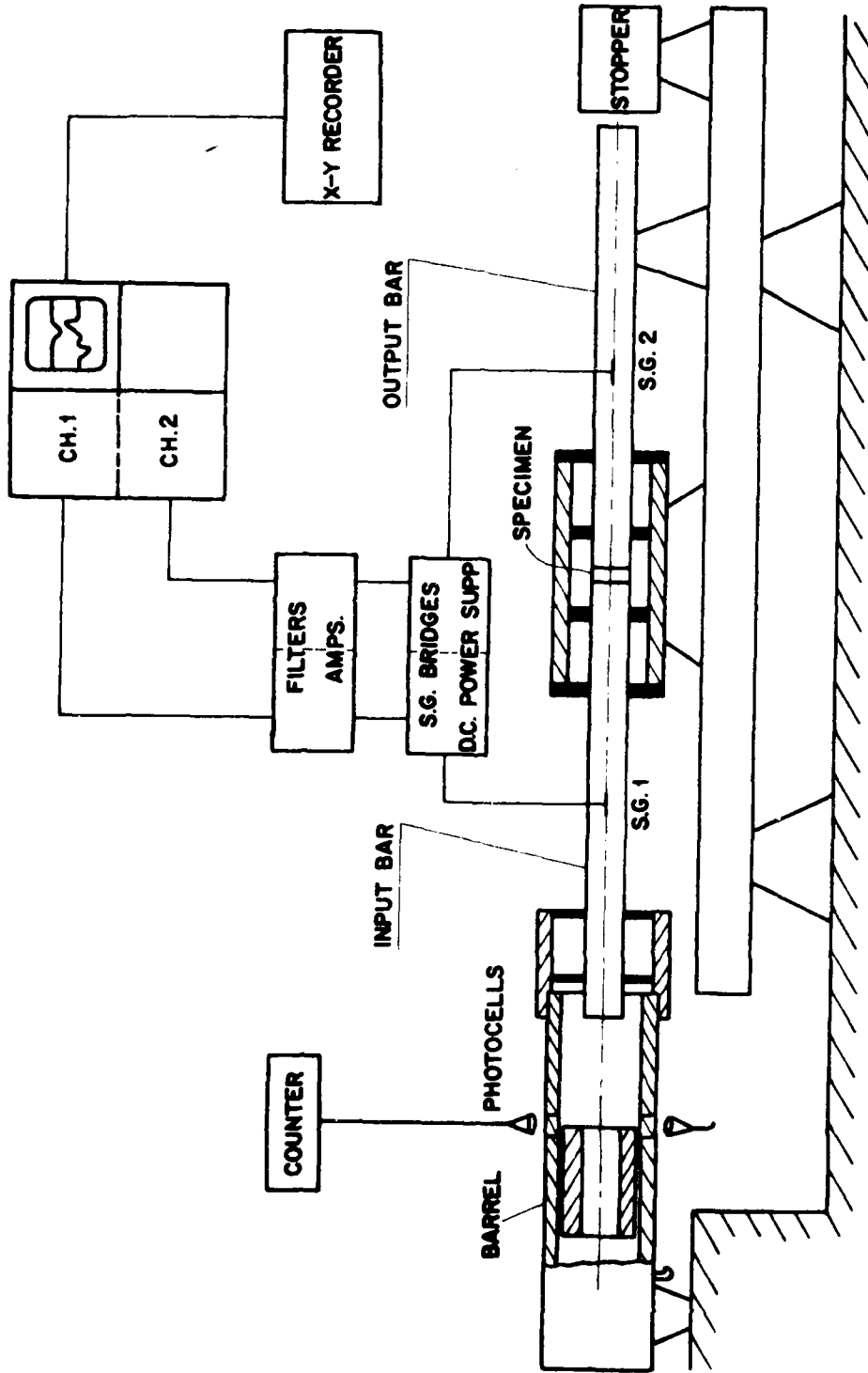


Fig. 1 : Schematic diagram of a split Hopkinson bar arrangement and instrumentations.

- Δ $\dot{\epsilon}_{avg} = 7.5 \cdot 10^{-4} \text{ [sec}^{-1}\text{]}; \text{ REF. [65]}$
 - x $\dot{\epsilon}_{avg} = 4.5 \cdot 10^3 \text{ [sec}^{-1}\text{]}; v_0 = 21.4 \text{ [m/sec]}$
 - o $\dot{\epsilon}_{avg} = 7 \cdot 10^3 \text{ [sec}^{-1}\text{]}; v_0 = 31 \text{ [m/sec]}$
 - $\dot{\epsilon}_{avg} = 1 \cdot 10^4 \text{ [sec}^{-1}\text{]}; v_0 = 36 \text{ [m/sec]}$
- EXPERIMENTAL RESIDUAL STRAIN

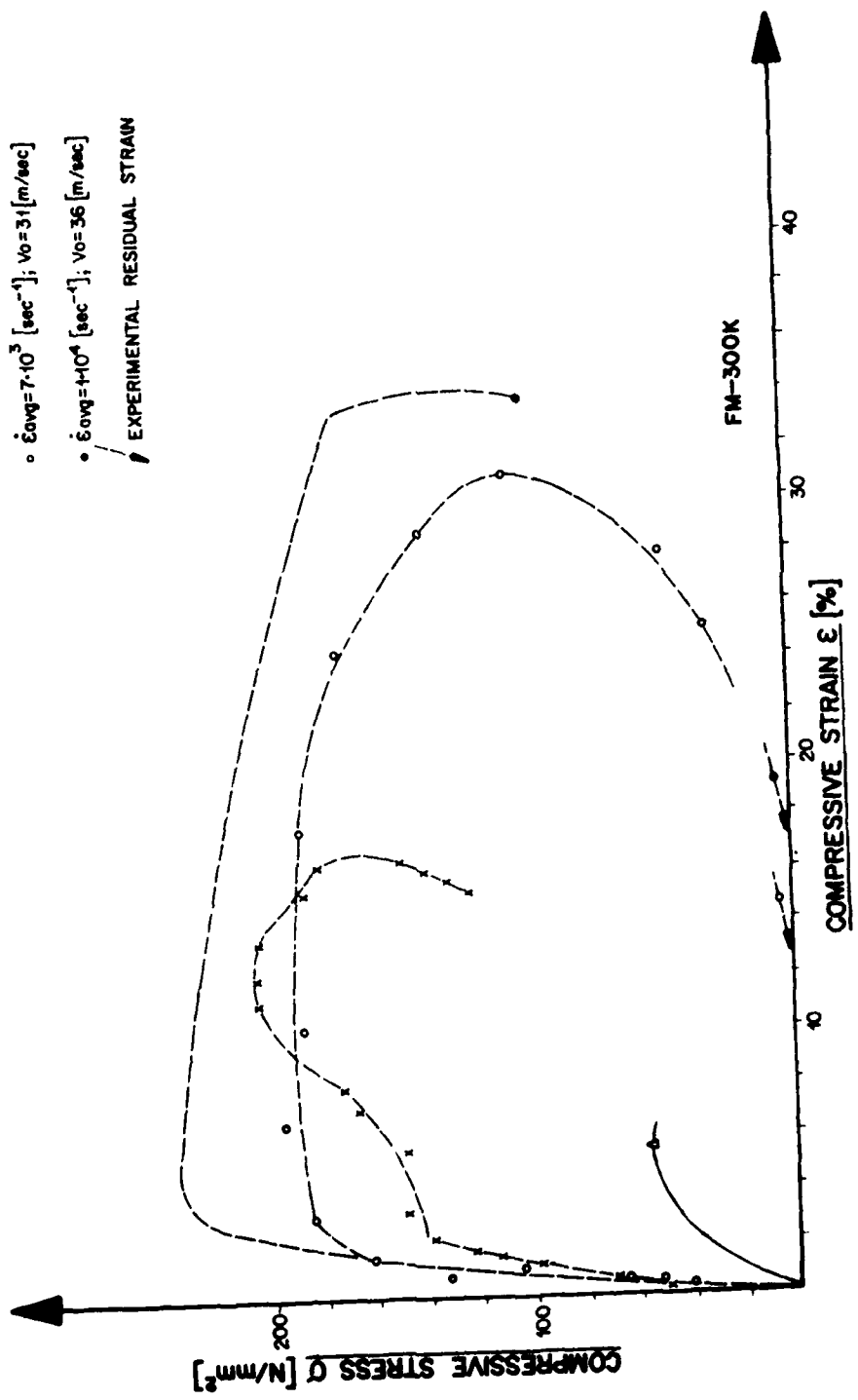


Fig. 2 : Typical results of stress-strain curves from "static" tests and under high rates of strain - FM-300K.

- △ $\dot{\epsilon}_{avg} = 7.5 \cdot 10^{-3} \text{ [sec}^{-1}\text{]}; \text{ REF. [33]}$
 - $\dot{\epsilon}_{avg} = 7.5 \cdot 10^{-3} \text{ [sec}^{-1}\text{]}; \text{ REF. [33]}$
 - × $\dot{\epsilon}_{avg} = 3 \cdot 10^3 \text{ [sec}^{-1}\text{]}; v_0 = 16 \text{ [m/sec]}$
 - $\dot{\epsilon}_{avg} = 5 \cdot 10^3 \text{ [sec}^{-1}\text{]}; v_0 = 26 \text{ [m/sec]}$
- EXPERIMENTAL RESIDUAL STRAIN

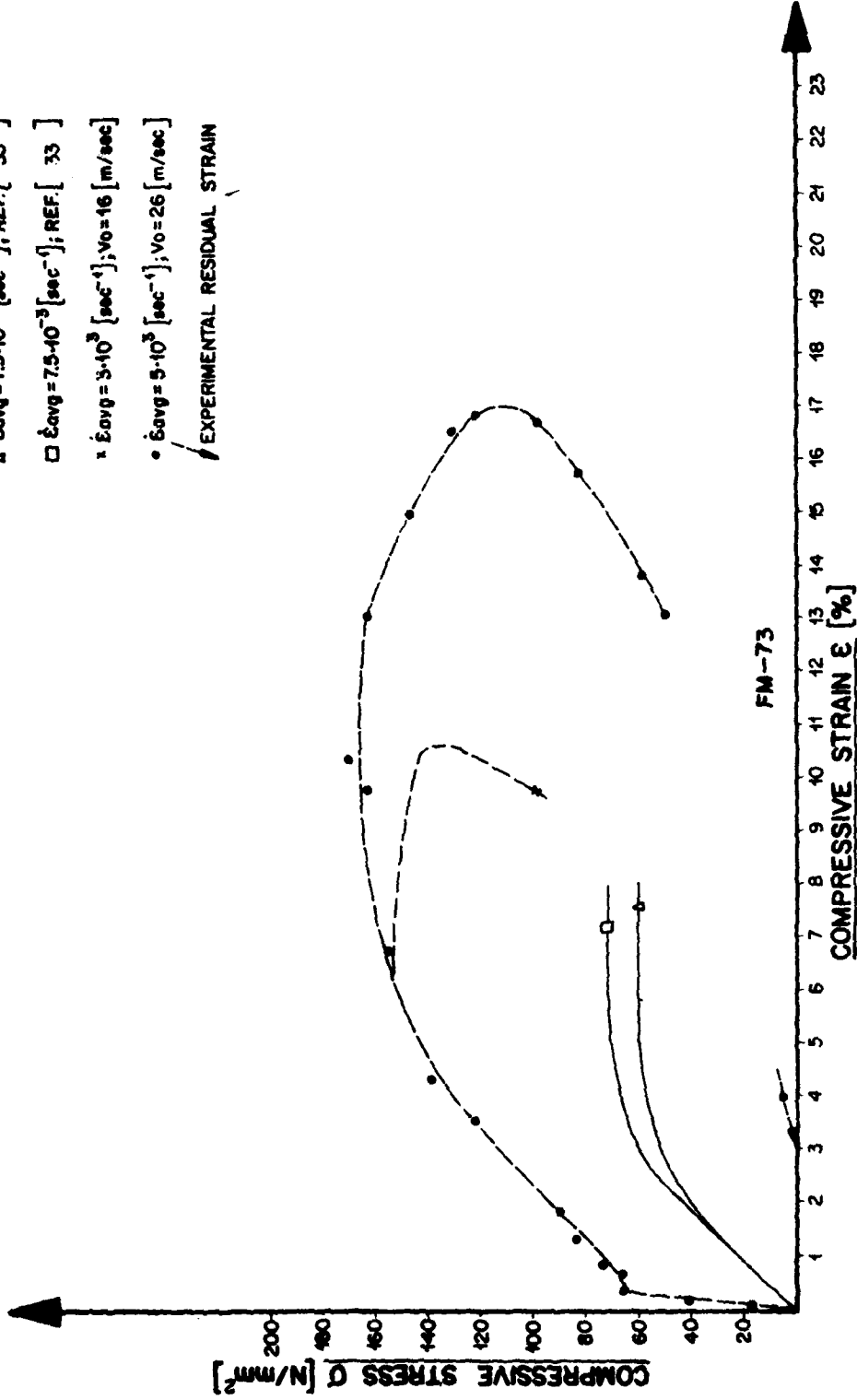


Fig. 3 : Typical results of stress-strain curves from "static" tests and under high rates of strain - FM-73.

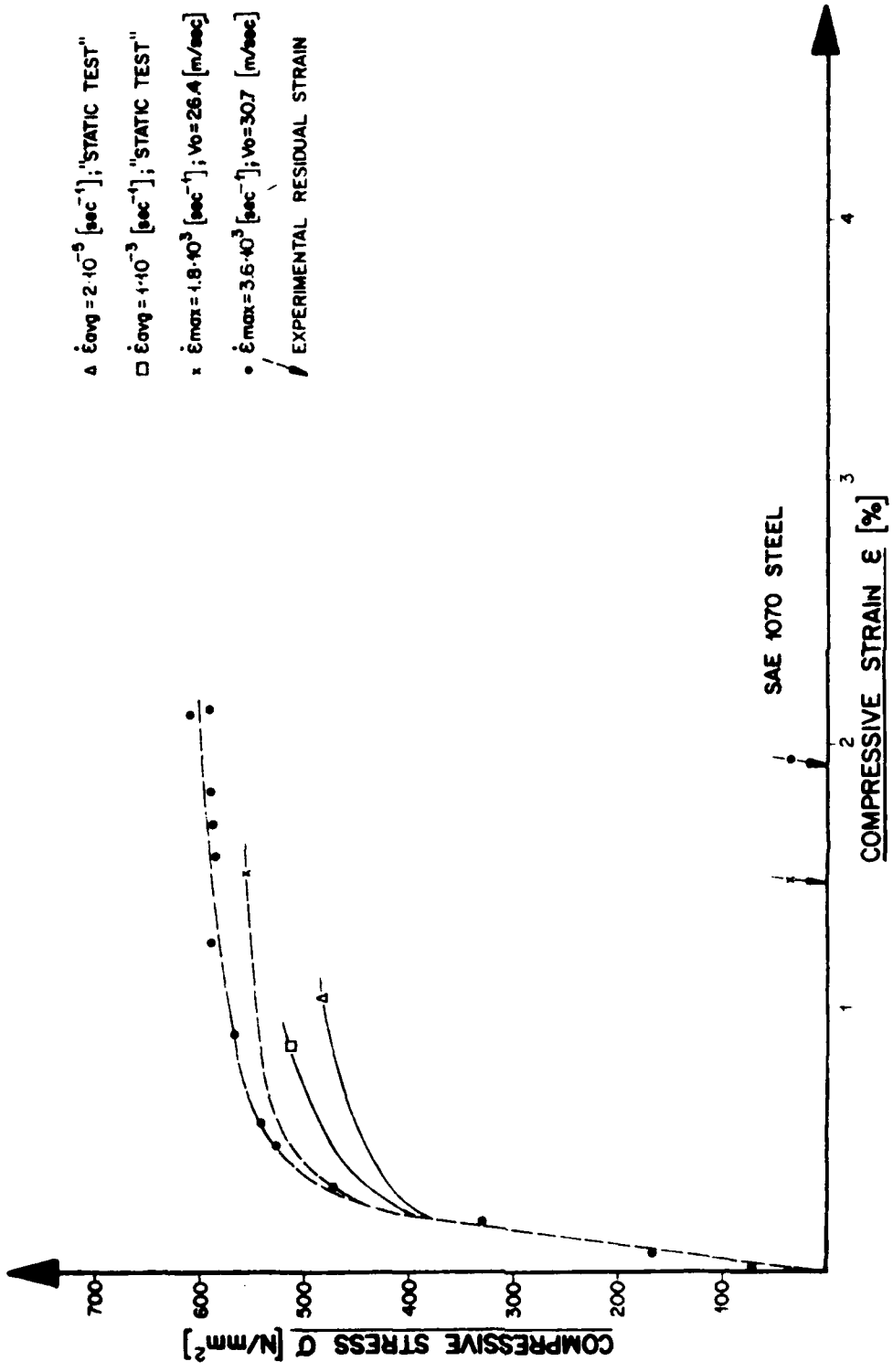


Fig. 4 : Typical results of stress-strain curves from "static" tests and under high rates of strain - SAE 1070 steel.

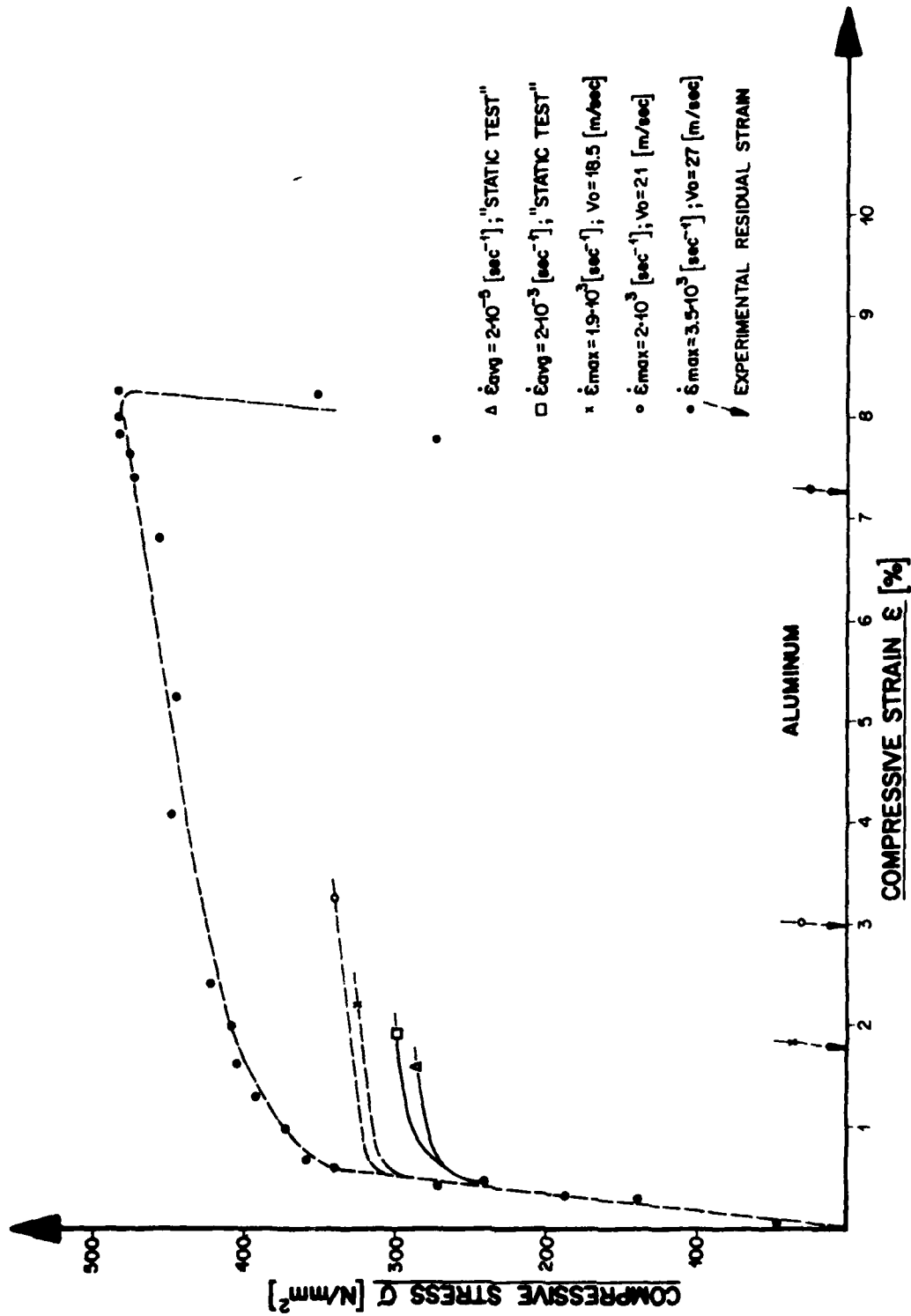


Fig. 5 : Typical results of stress-strain curves from "static" tests and under high rates of strain - Aluminum 2011-T3.

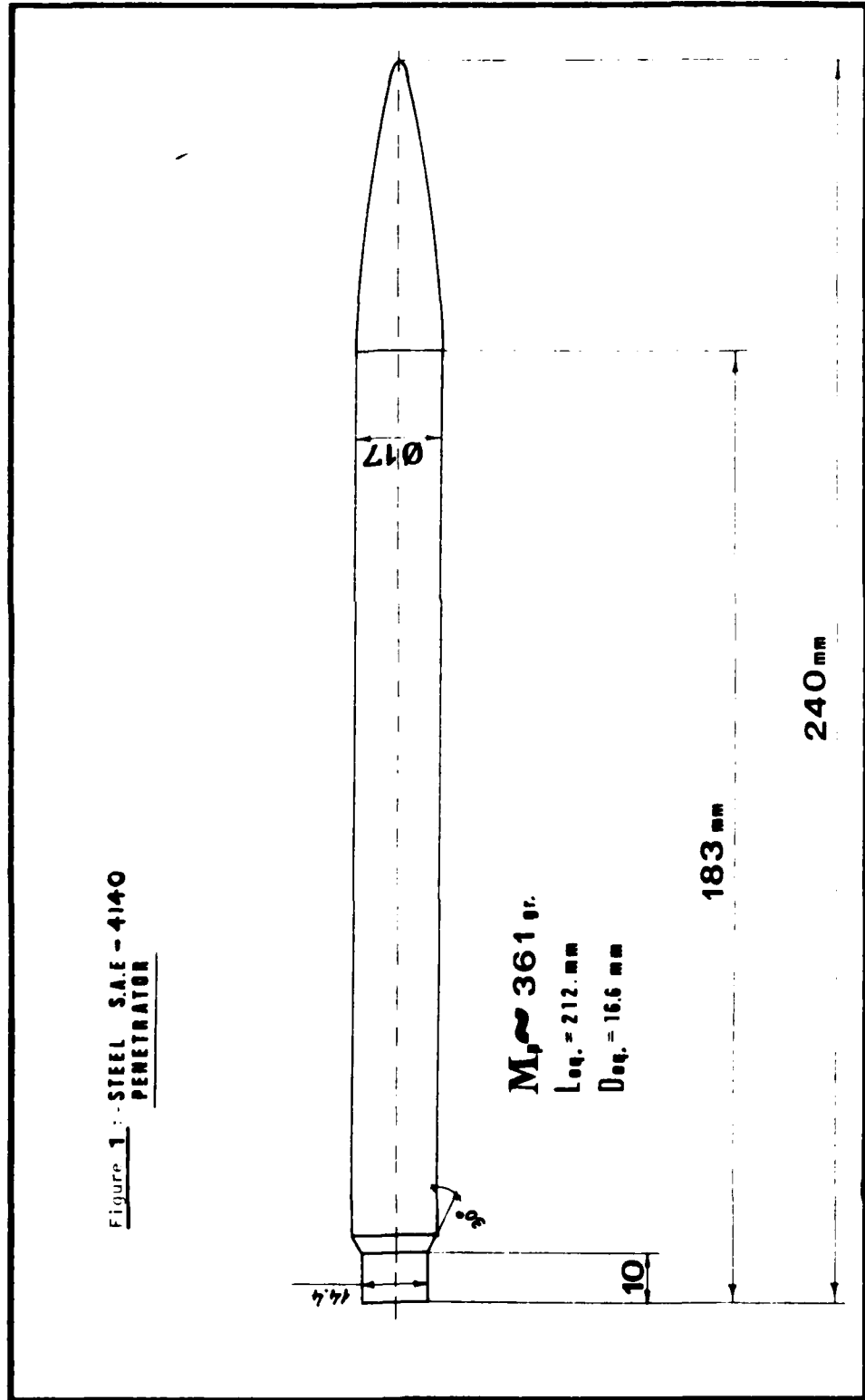


Figure 1 - STEEL S.A.E - 4140
PENETRATOR

Table I : Penetrator Material Description. SAE 4140 [EN 19A]

Symbol	C	Si	Mn	P	S	Cr	Mo
[%]	0.41	0.21	0.72	0.015	0.022	1.06	0.22

Table II : Mechanical Properties of Penetrator Material.

Yield Stress Y_P	Ultimate Stress U.T.S.	Elongation ϵ_{max}	Impact Test IZOD
$Kg\ f/mm^2$	$Kg\ f/mm^2$	%	$Kg\ f \cdot m$
78 - 80	90 - 91	22 - 24	11 - 13

Table III: Target Plates and Mechanical Properties of Target Material.

Plate Material	Plate Thickness	Mechanical Properties - (*)		
		Yield Stress	Ultimate Stress	Max. Strain
	T	$Y_P (\sigma_{0.2})$	U.T.S.	ϵ_{max}
	mm	$Kg\ f/mm^2$	$Kg\ f/mm^2$	%
R.H.A. (**)	50.8	86	97-98.7	15.1-15.3
R.H.A. (**)	75	80-85	91.3-98.6	15.3
AL-5083 H-115	44.5	11-12	26.2-28.2	15.8-18.3

(*) At Strain-Rate of $\sim 0.1\ Sec^{-1}$ for Steel and $\sim 0.6\ Sec^{-1}$ for Aluminum Plates (obtained on M.T.S. machine, 25 ton capacity).

(**) According to Mil-S-12560B (ORD)

Table IV : Summary of Before Target Penetration Results and Analysis.

Round Number	Target Description	Striking velocity (m/sec) V_s			Trajectory Components (Degree)		Impact Angle (Degree) (Note 1)	Yaw Components (Degree)		Yaw Angle (Degree)
		Photo-electric Cell Results	Flash X-ray Average Results	Mean Striking velocity	Horizontal	Vertical		Horizontal	Vertical	
11	75 mm	1560	1550	1555	-0.29	0.87	~1	0.22	0.04	0.23
12	R.H.A	1430	1454	1442	-	0.74	~1	-	0.25	~0.3
13		1357	1355	1356	-0.06	0.82	~1	-0.55	-0.6	0.7
14	50.8mm	1560	1549	1555	-0.31	-	~1	0.74	-	~0.8
15	R.H.A.	-	1461	1461	0.39	-	~1	0.08	-	~0.1
16		1390	1383	1387	-0.61	-	~1	-0.4	-	~0.4
19	133.5mm	-	1560	1560	-	1.03	~1	-	0.72	~0.8
20	AL5083	1391	1387	1388	-0.64	0.84	~1	0.12	0.15	0.2

Table V : Summary of After Target Perforation Results and Analysis.

Round Number	Target Description	Penetration Duration (10 ⁻⁶ sec)	V _P		Vertical Yaw Component (Degree)	L _R	M _R	Penetrator front Deformation	
			Residual Velocity (M/sec)	Vertical Trajectory Component (Degree)				*H _f Length (mm)	**D _{jf} Diameter (mm)
11	75mm	159	1342	-0.8	0.2	96	197	12	24
12	R.H.A.	239	1117	-3.1	22.9	65	117	12	19
13		350	215	7.7	-39	25	102	Plug P.L. 13	Plug P.D. 19
14	50.8mm	135	1405	-0.6	3.3	146	296	9	25
15	R.H.A.	163	1310	-0.5	7	125	255	10	20
16		182	1240	-0.8	1.8	130	259	9	23
1a	133.5mm	244	1390	1.1	-4.3	138	303	10	13
20	ALC83	270	1218	0.1	0.4	136	270	14	22

*H_f - Length of forward end of penetrator that is subjected to appreciable plastic deformation.

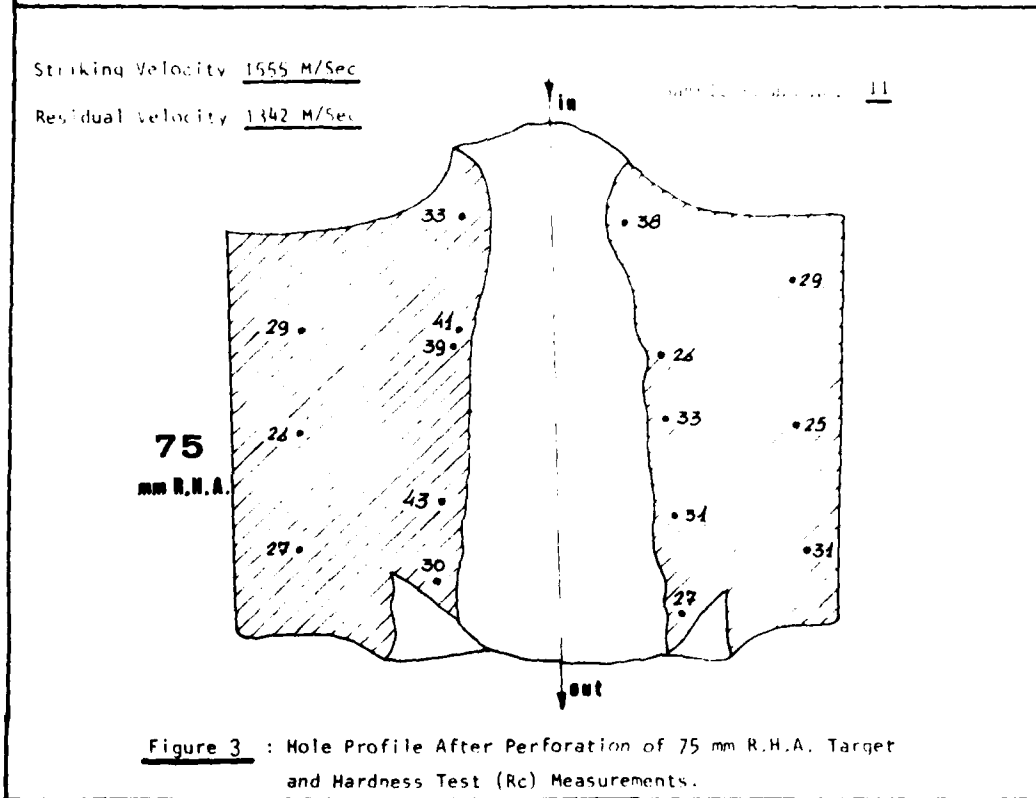
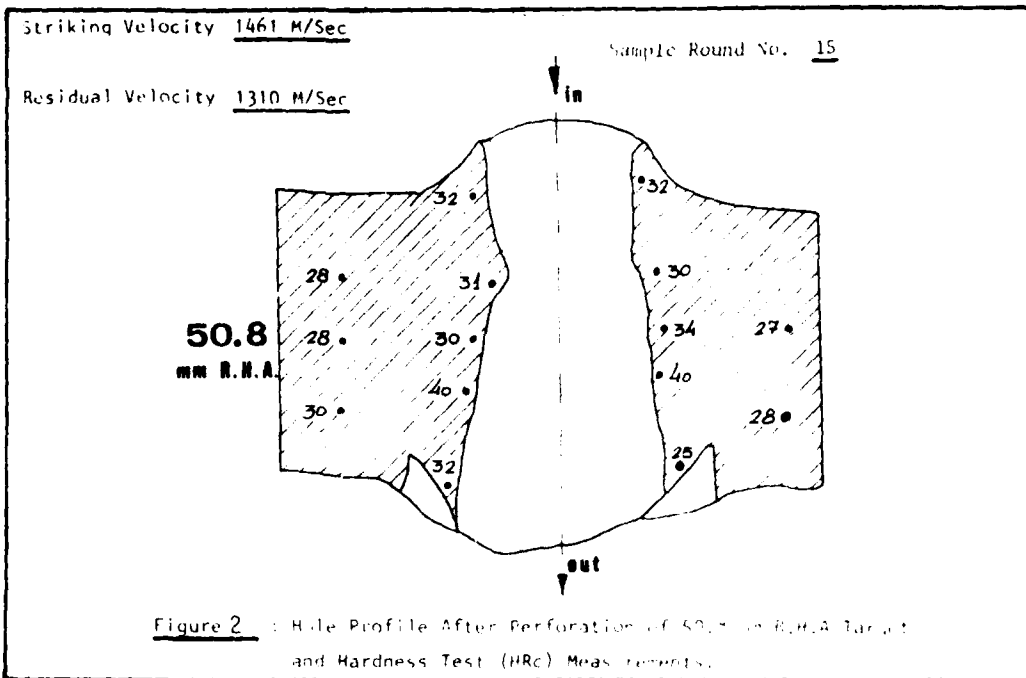
**D_{jf} - Maximum diameter of plastically deformed forward end of projectile.

Table VI . Summary of Target Hole Dimension Measurements

Round Number	Target Description	D _i Target Entrance Hole Average Diameter (mm)	D _e Target Exit Hole Average Diameter (mm)	Exit Circumferential Fracture	
				*D _{fr} Average Diameter (mm)	**P _{fr} Average Depth (mm)
11	75mm R.H.A.	20	37	61	16
12		19	36	58(Partial)	11
13		20	37	49(Partial)	10
14	50.8mm R.H.A.	19	35	55	9
15		20	36	57	8
16	133.5mm AL5083	Depth 20	35	47	9
19		44.5	27	Ductile Exit	
		89	38		
	133.5	48			
20	133.5mm AL5083	44.5	22	Ductile Exit	
		89	34		
		133.5	39		

*D_{fr} - Maximum diameter of circumferential fracture region surrounding exit hole (circumferential avg.).

**P_{fr} - Depth from rear surface of circumferential fracture region surrounding exit hole (circum. avg.).



Striking Velocity 1560 M/Sec

Sample Round No. 19

Residual Velocity 1390 M/Sec

133.5 mm

AL-5083

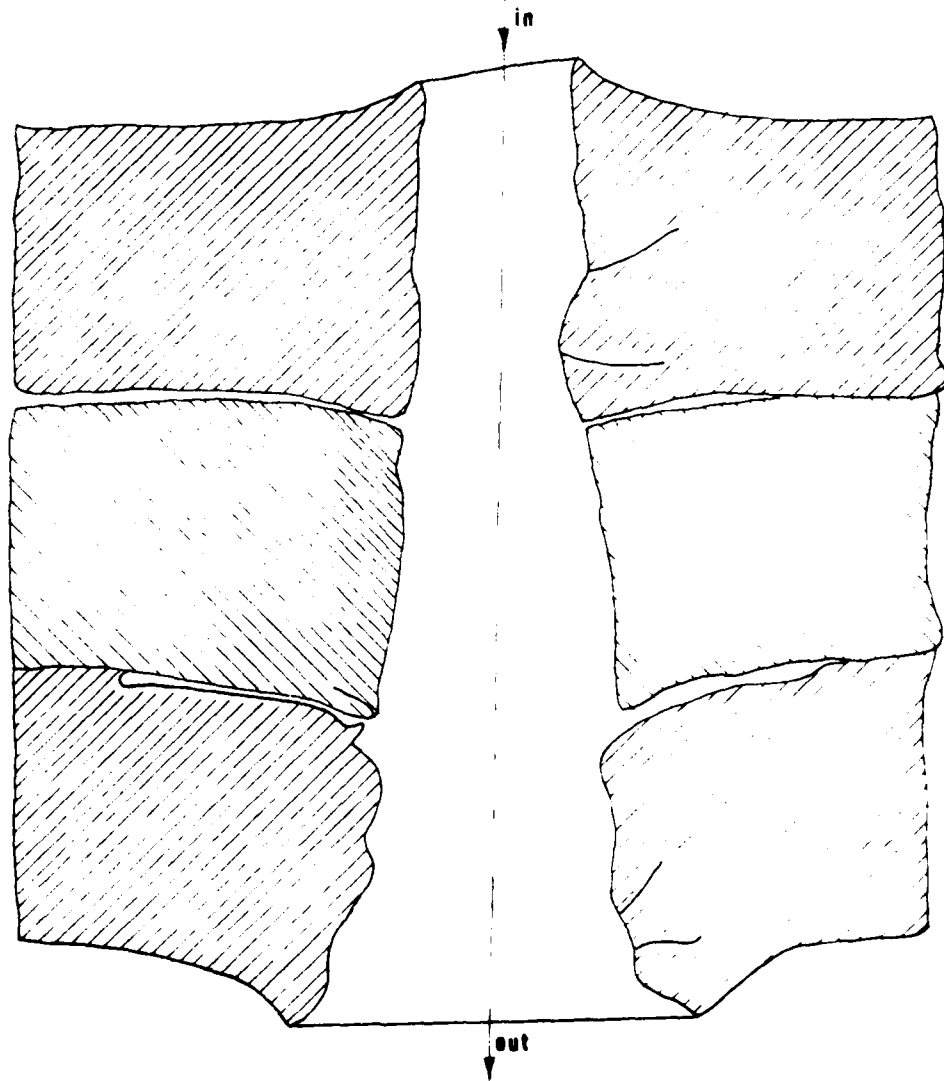
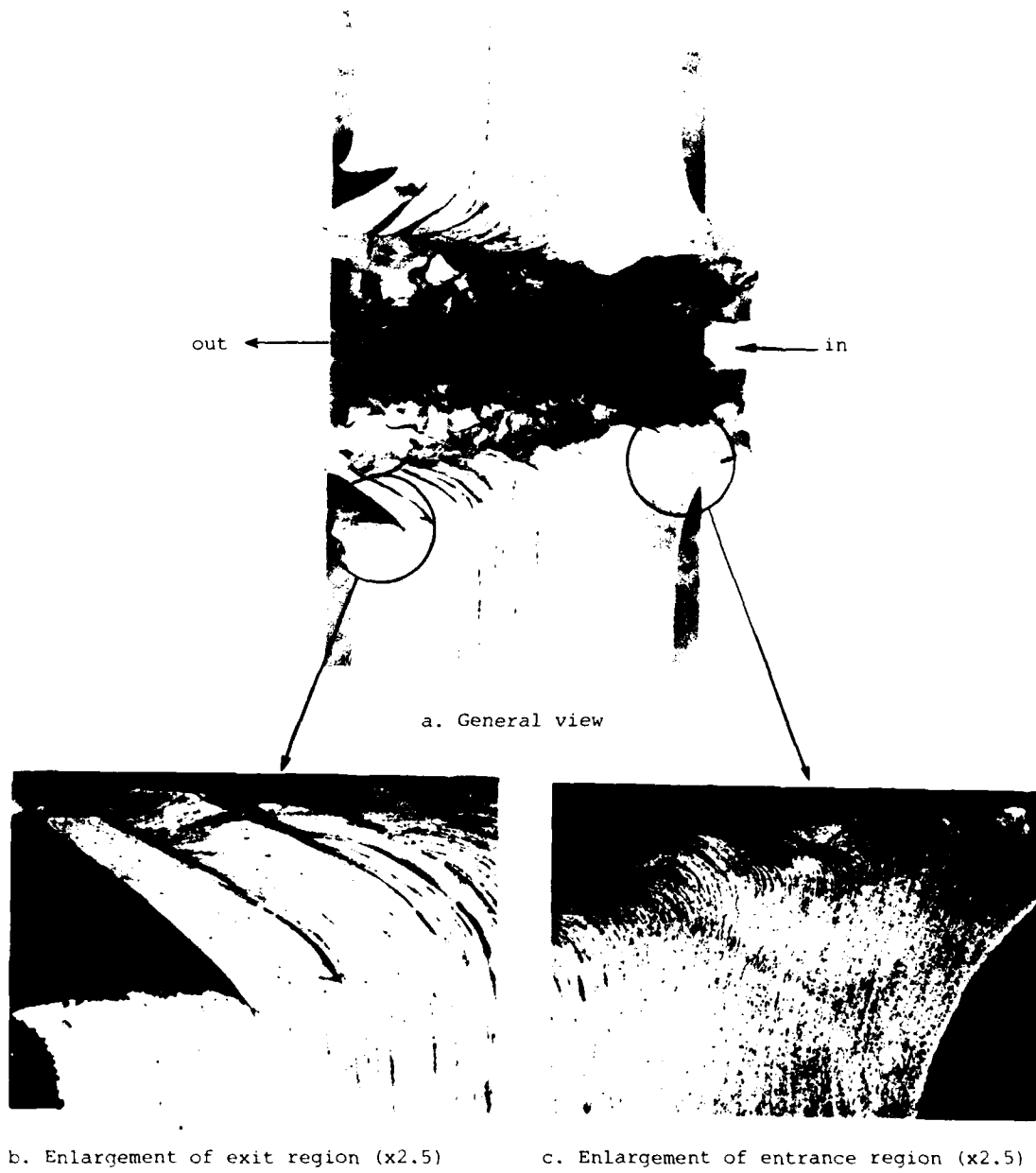


Figure 4 : Hole Profile, After Perforation of 133.5 mm AL 5083 H-115
Target (3 x 44.5 mm)



b. Enlargement of exit region (x2.5)

c. Enlargement of entrance region (x2.5)

Etching: Boiling 50% HCl

Figure 5: Hole profile after perforation of 50.8 mm R.H.A. target.

(Round No. 15; $V_S = 1461$ m/sec; $V_R = 1310$ m/sec; $L_R = 129$ mm)

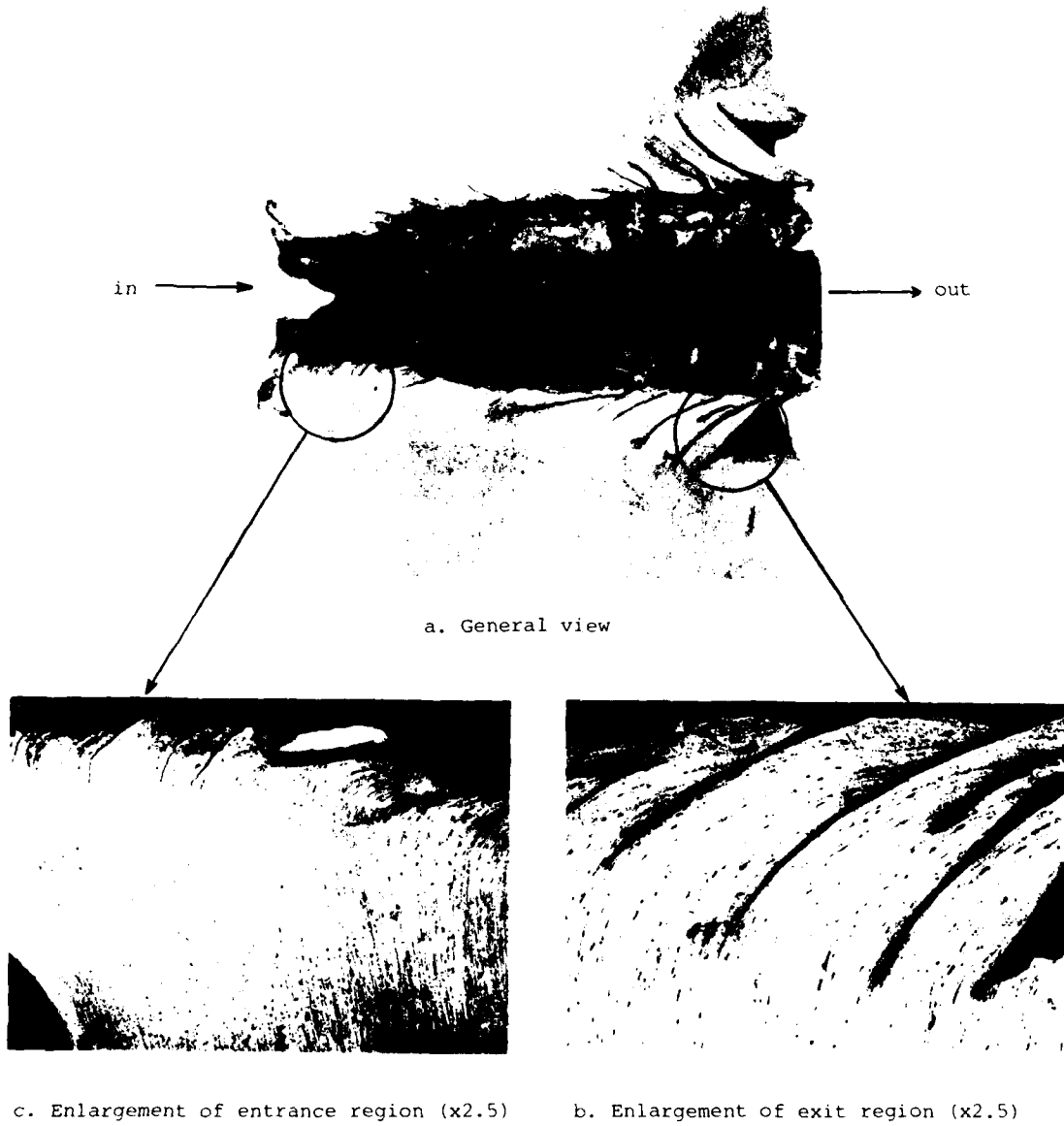
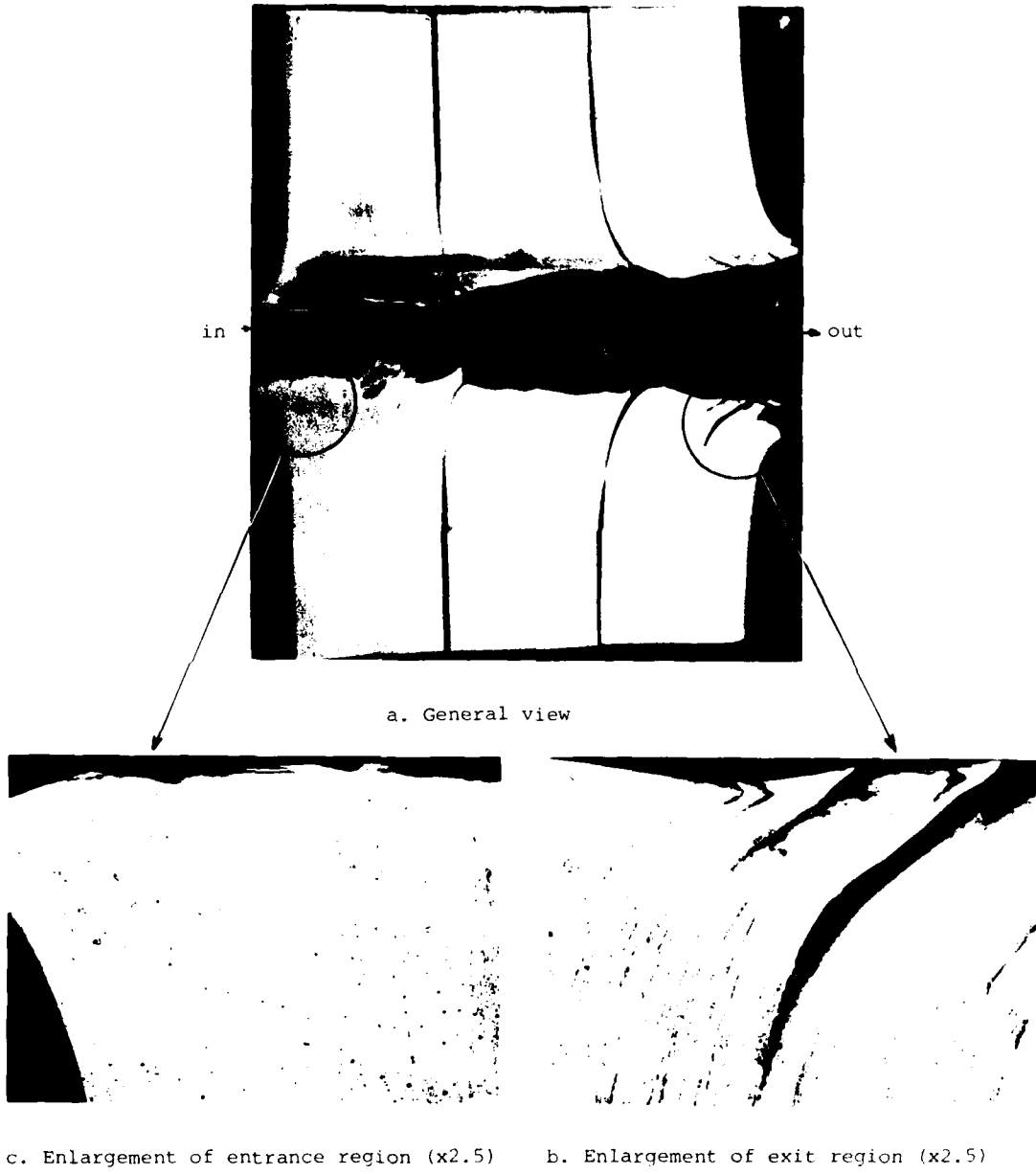


Figure 6: Hole profile after perforation of 75 mm R.H.A. target.

(Round No. 11; $V_S = 1555$ m/sec; $V_R = 1342$ m/sec; $L_R = 96$ mm)



Etching: Feric Chloride + HCl + Alcohol

Figure 7: Hole profile after perforation of 133.5 mm AL 5083 H-115 target.
(Round No. 20; $V_S = 1388$ m/sec; $V_R = 1218$ m/sec; $L_R = 136$ mm)



Etching: Feric Chloride + HCl + Alcohol

Figure 8: Hole profile after perforation of 133.5 mm AL 5083 H-115 target.

(Round No. 19; $V_S = 1560$ m/sec; $V_R = 1390$ m/sec; $L_R = 138$ mm).

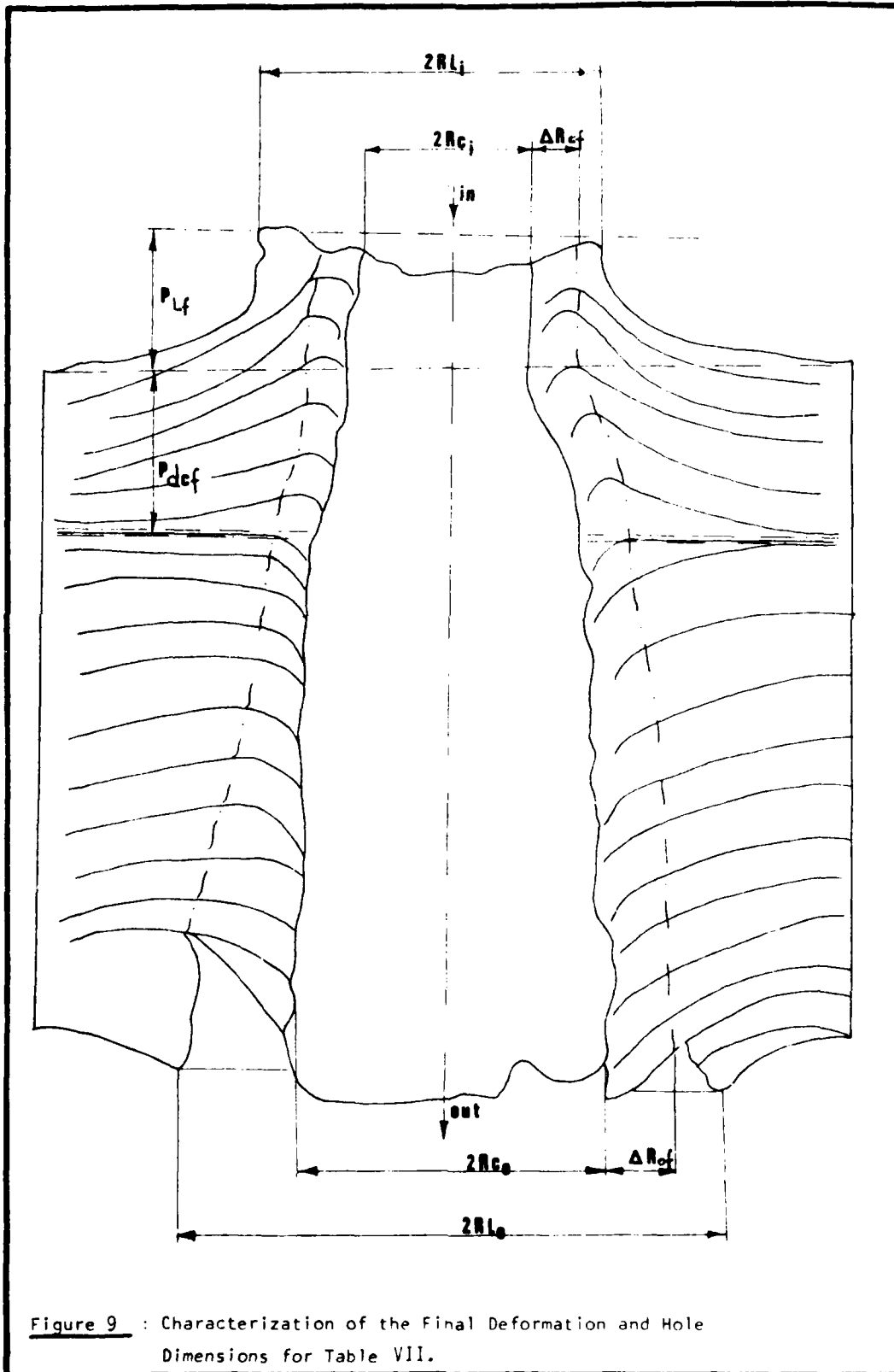


Table VII: Characteristic Parameters Measured for Defining the Final Target Deformation

Round Number	Target Description	Entrance Lips - P_{Lf} (mm)	Depth of Entrance Deformation - P_{dcf} (mm)	Radial Clearance for Sheared Regions (mm)	
				ΔR_{cf} Entrance	ΔR_{of} Exit
15	50.8mm R.H.A.	8.8 - 10.8	11.1 - 14.8	3.4	8.3 - 8.4
11	75mm R.H.A.	9.0 - 12.1	13.4 - 15.9	3.5-4.5	10.4-10.8
20	133.5mm AL5083	7.8 - 10.4	17.8 - 18.0	5.1	12.6-14.1
		9.5 - 11.5	19.9 - 20.7	5.8-6.5	11.6-12.9

DYNAMIC PERFORATION OF VISCOPLASTIC PLATES
BY RIGID PROJECTILES*

by

M. Ravid and S. R. Bodner
Faculty of Mechanical Engineering
Technion - Israel Institute of Technology
Haifa 32000 Israel

Abstract

A model is formulated for the dynamic perforation of viscoplastic plates by rigid projectiles. The process is considered to occur in five continuously coupled but distinct stages which are amenable to analytical treatment. An essential feature of the analysis is the use of postulated, physically motivated, deformation mechanisms in conjunction with the upper bound theorem of plasticity theory which is modified to include dynamic effects. Special attention is given to the bulging process and effects associated with the later stages. This model is self-contained and capable of predicting the exit velocities of the projectile and the plug. It also determines the bulge and plug shape, provides the force-time history of the process, and describes a number of geometrical features of the transient and final deformation state of the target plate.

*The research work reported in this paper has been sponsored in part by the U.S. Army (European Research Office, London) under Contract DAJA37-81-C-0047.

Introduction

During the penetration and perforation process of a rigid cylindrical rod in a metallic target plate, the target material undergoes extensive plastic deformation due to the high pressure developed by the penetrator/target interaction. After a short, high pressure impact phase which could exist for about a microsecond, a stable, steadily growing plastic flow field develops in the target. This flow field has a major influence on the penetration process since it governs the resistance to penetration in the initial stage prior to the onset of bulging and is also an important factor on the exit of the projectile. In previous engineering models of penetration, e.g. [1], the static and dynamic effects of the flow field have been considered in a very approximate and overall manner which required the use of some empirical factors. In addition, the dynamic effects that have to be taken into account in an overall approach are not entirely obvious as has been discussed by Tate [2]. Another limitation of the simplified model is the difficulty of properly incorporating the influence of material strain-rate dependence. Despite these shortcomings, the simplified three stage model of [1] has been reasonably successful in predicting the most important features of the perforation process [7].

In this paper, the process is analyzed by means of a five stage sequence of deformation mechanisms shown in Fig.1. These are 1. dynamic plastic penetration, 2. bulge formation, 3. bulge advancement, 4. plug formation and exit, and 5. projectile exit. The first, principal, stage involves the determination of an approximate plastic flow (velocity) field surrounding the projectile at each increment of penetration and includes the development of a "lip" on the entry surface of the target. Material strain-rate dependence is considered in obtaining the associated stresses and the work rate terms. Certain parameters that characterize the field of stage 1 are determined by utilizing a modification of the upper bound theorem of plasticity to include dynamic effects.

A plastic flow velocity field is also assumed for each of the later stages with parameters introduced to describe the geometrical features of the deformation mechanism under consideration. In these cases, the parameters are obtained directly from the mechanics of the situation without the need for prior test information or minimization procedure. The resultant flow field, in turn, determines the forces that resist the perforation process. The improved engineering model presented in this paper is essentially self-contained and can provide adequate analytical treatment of the various physical phenomena associated with perforation.

Input data consists of the projectile diameter, length, density, and impact velocity, and the mechanical properties, density and thickness of the target material. The predictions based on this information are the time histories of the projectile velocity and displacement and of the resisting force, and also the history of the plastic deformation state of the target plate including the entry "lip", the rear surface bulge, and the plug shape. In addition, the analysis gives the exit velocities of the projectile and the plug. Since the projectile is assumed to be rigid, flattening is not taken into account although the general method can be extended to include this effect. A flat ended projectile is considered for simplicity, while other nose geometries would require modification of the plastic velocity field but would not cause any essential difficulty in the calculations.

General Formulation

The general procedure for analyzing the various stages of perforation is to assume a plastic flow velocity field that describes the particular mechanism. This field would be required to meet the kinematical constraints and the compatibility and incompressibility conditions and, in some cases, would initially contain certain undetermined parameters. Those parameter values would be obtained by minimizing the expression for the rate of plastic work, i.e. the energy dissipation rate, at each increment of penetration. Convective inertia terms arising from the motion of the target material, i.e. terms proportional to the square of the velocity, are taken to be part of the dissipation function to be minimized. On the other hand, the local inertia terms, which are proportional to the acceleration, are treated as an "effective mass" of material acting together with the projectile and therefore not subject to the minimization process.

This procedure can be rationalized on the basis of Martin's 1972 theorem on acceleration fields [3] which states that the rate of work of the inertial force based on an assumed acceleration field would be an upper bound on the actual one. Alternatively, the upper bound theorem of plasticity, in the absence of applied forces, can be interpreted as applying to the inertial force consisting of the

projectile and "effective mass" of target material multiplied by their respective accelerations. In problems involving prescribed forces acting on plastic media, e.g. the dynamic punch problem, the material acceleration terms would be part of the expression to be minimized based on direct application of the upper bound theorem. That was the method employed by Tirosh and Kobayashi in [4].

To obtain the strain rates $\dot{\epsilon}_{ij}$ from the velocity field, the conventional relation is used,

$$\dot{\epsilon}_{ij} = (1/2)(v_{i,j} + v_{j,i}), \text{ where } \dot{\epsilon}_{kk} = 0 \quad (1)$$

The target material is assumed to be rigid-plastic with the flow stress a function of strain rate. Work hardening can be considered indirectly by taking the flow stress to be the average value, with respect to plastic work, over the full strain range. Strain rate dependence of the flow stress is introduced by a logarithmic relation which has been used by a number of investigators, e.g. Lindholm [5], and is convenient for the perforation problem,

$$\sigma_y = \sigma_0 [1 + C \log_{10} \dot{\epsilon}^{eff}] = \sigma_0 S(\dot{\epsilon}) \quad (2)$$

In this expression, σ_0 is the reference "static" flow stress (actually corresponding to $\dot{\epsilon}^{eff} = 1$), the material constant C is taken in practice to be zero for strain rates lower than unity, and σ_y is

the flow stress corresponding to the effective plastic strain rate (calculated in the usual manner).

Total plastic work rate in a volume zone V_n can be expressed as

$$\dot{W}_V^n = \int_{V_n} \sigma_{ij} \dot{\epsilon}_{ij} dV = (\sigma_Y)_n \dot{\epsilon}_n^{eff} V_n \quad (3)$$

where $(\sigma_Y)_n$ is the flow stress corresponding to the average effective plastic strain rate over the volume V_n , $\dot{\epsilon}_n^{eff}$, defined by

$$\dot{\epsilon}_n^{eff} = [(\sqrt{2/3})/V_n] \int_{V_n} \sqrt{\dot{\epsilon}_{ij} \dot{\epsilon}_{ij}} dV \quad (4)$$

For zone boundaries with a tangential velocity discontinuity Δv_i across a surface A_m , i.e. a shear velocity, the plastic work rate is

$$\dot{W}_S^m = [(\sigma_Y)_m/\sqrt{3}] \int_{A_m} |\Delta v_i| dA \quad (5)$$

When the surfaces are the interfaces between flow zones, the stress $(\sigma_Y)_m$ is taken to be the minimum value for the zones. Friction losses \dot{W}_F^m due to relative motion between the projectile and the adjacent target material can also be represented by (5) with a friction coefficient μ that could vary between 0 and 1. For greater generality, these coefficients are taken to be different on the frontal and lateral faces of the projectile and designated μ_f and μ_l

respectively. In practice, the overall influence of the frictional forces is small during stages 1 to 4. They are the dominant factor for stage 5 and the coefficients are obtained from the available information, e.g. dynamic punching tests.

The dissipative work rate due to the internal stresses and frictional forces would then be quantities \dot{W}_V^n , \dot{W}_S^m and \dot{W}_f^m summed over the volumes and areas over which they are acting. These quantities can be non-dimensionalized by dividing by $\pi R^2 v \sigma_0$ where R is the radius of the projectile (Fig.2), and v is its current velocity, e.g.

$$\dot{W}'_V = \frac{\sum \dot{W}_V^n}{\pi R^2 v \sigma_0} ; \dot{W}'_S = \frac{\sum \dot{W}_S^m}{\pi R^2 v \sigma_0} ; \text{etc.} \quad (6)$$

The work rate of the inertial forces in the zone V_n due to the motion of target material is given by

$$\dot{W}_I^n = \dot{W}_k^n + \dot{W}_d^n = \rho_t \int_{V_n} \dot{v}_i v_i dV \quad (7)$$

where \dot{W}_k^n is the kinetic work rate and \dot{W}_d^n is the dynamic work rate and ρ_t is the mass density of the target. The total acceleration consists of the local and convective components,

$$\dot{v}_i = \frac{D}{Dt}(v_i) = \frac{\partial}{\partial t}(v_i) + (v_i \cdot \nabla) v_i \quad (8)$$

Upon determining \dot{v}_i from (8) and expressing the material velocities in the plastic zones, v_i , as functions of the projectile velocity v and the geometry, the inertial work rate can be decomposed in the form of (7). Non-dimensionalizing the inertial work rate terms by dividing by $\pi R^2 v \sigma_0$, leads to

$$\dot{W}'_k = (\rho_t v^2 / \sigma_0) g_1 \quad (9)$$

$$\dot{W}'_d = (\rho_t \dot{v} R / \sigma_0) g_2 \quad (10)$$

It is noted that the non-dimensional kinetic work rate is proportional to v^2 and the dynamic work rate to \dot{v} . The functions g_1 and g_2 in (9,10) depend upon non-dimensional geometrical parameters of the flow field.

For a flat nosed, cylindrical projectile, the work rate of the total force acting on it in the negative velocity direction is given by

$$\dot{W}'_p = - \rho_p \pi R^2 L \dot{v} v \quad (11)$$

or, in non-dimensional form,

$$\dot{W}'_p = - \rho_p L \dot{v} / \sigma_0 \quad (12)$$

where ρ_p is its mass density. The energy rate balance equation for the complete system is therefore

$$\dot{W}'_p = \dot{W}'_v + \dot{W}'_s + \dot{W}'_f + \dot{W}'_k + \dot{W}'_d \quad (13)$$

or, using (10) and (12),

$$-[\rho_p L + \rho_t R g_2](\dot{v} / \sigma_0) = \dot{W}'_T \quad (14)$$

where

$$\dot{W}'_T = \dot{W}'_v + \dot{W}'_s + \dot{W}'_f + \dot{W}'_k \quad (14a)$$

Equation (14) can be interpreted as a simple dynamical equation of motion in which the total mass is that of the projectile plus an effective mass of target material. Another, and different, effective mass term appears in the expression for \dot{W}_k' . In this respect, the analysis is similar to that of [1] but the various terms are obtained from more fundamental considerations.

As discussed previously, it may be necessary in certain cases, e.g. stage 1, to obtain certain geometrical parameters by minimizing the energy dissipation terms on the right hand side of eq.(14), \dot{W}_T' , at each displacement increment. This will determine \dot{v} , and a simple iterative procedure is used to obtain the projectile velocity v and time for the next increment in displacement Δx . For the other stages, all the geometrical parameters of the assumed flow field are obtained from the kinematic, continuity and incompressibility conditions. A typical complete calculation of the perforation process requires about 10 minutes on a minicomputer, e.g. Digital PDP 11/44. Detailed descriptions of the velocity fields and analytical procedures for each of the stages are given in the following sections.

Stage 1 - Dynamic Plastic Penetration

This stage would develop very shortly after initial impact and is characterized by continuously growing plastic zones surrounding the projectile. An approximate, axisymmetric velocity field that satisfies the geometrical compatibility conditions was suggested by Iddan and Tirosh [6] for the punch problem and is used in this analysis, Fig.2. The velocity components in cylindrical coordinates for the various flow zones and the corresponding strain rates from eq.(1) are given in Table 1. Velocities normal to a zone boundary are required to be continuous across the interface while discontinuities in the tangential direction lead to shear energy dissipation, eq.(5). To maintain zero volume change, material in zone III must move opposite to the direction of penetration leading to "frontal petalling" of the entry surface, H_L .

The longitudinal extent of the plastic zone ahead of the projectile at a penetration distance x is given by αR while the plastic zone radius is ηR , Fig.2, where α and η are obtained by minimizing \dot{W}'_T , eq.(14a), at each increment of penetration Δx . This stage will end when the plastic zone depth reaches the rear surface of the target plate, i.e. $x + \alpha R = H$, for which $x = x_0$. At this condition, $\eta = \eta_0$ where $\eta_0 R$ is the maximum radius of the plastic zone and also the maximum extent of the shear zone in subsequent stages, so that the shear zone width e defined in [1,7] would correspond to $R(\eta_0 - 1)$ in this treatment.

In order to use the strain rate dependence of the yield stress, eq. (2), average effective strain rates are calculated from eq. (4) for zones I and II giving, respectively,

$$\dot{\epsilon}_1^{\text{eff}} = (v/\alpha R) \quad (15)$$

$$\dot{\epsilon}_2^{\text{eff}} = (v/\alpha R) \frac{f_1(\eta)}{\sqrt{3}(\eta^2-1)^2} \quad (16)$$

where

$$f_1(\eta) = 2\eta^2 - \sqrt{\eta^4+3} + \eta^2 \ln\left[\frac{1}{3}(\sqrt{\eta^4+3} + \eta^2)\right] \quad (17)$$

For zones III and IV, the average effective strain rate is zero.

Calculation of the non-dimensional energy dissipation rate terms of (14a) for the velocity field described in Table 1 leads to the following expressions:

$$\dot{W}'_V = S_1 + S_2 \frac{f_1(\eta)}{\sqrt{3}(\eta^2-1)} \quad (18)$$

where $f_1(\eta)$ is given by (17), and S_1 and S_2 are the strain rate factors defined by (2) for zones I and II having the strain rates (15) and (16) respectively;

$$\dot{W}'_S = \frac{\eta}{\sqrt{3}(\eta^2-1)} \left\{ \alpha[1+\eta \min(S_1, S_2)] + \frac{(4\eta^3-5\eta^2+1)}{3\alpha\eta} + \frac{2x}{R} \right\} \quad (19)$$

$$\text{and } \dot{W}'_f = \frac{S_1 \mu_f}{3\sqrt{3}\alpha} + \frac{2\nu_s \eta^2}{\sqrt{3}(\eta^2-1)} \left[\frac{(x+H_L)}{R} \delta + \frac{L}{R} (1-\delta) \right] \quad (20)$$

where L is the projectile length and $\delta=0$ for $x \geq L-H_L$ while $\delta=1$ for $x < L-H_L$. The frontal lip height H_L is the accumulation of the incremental lifts of material in zone III at the forward face of the target, where $\Delta H_L = \Delta x / (\eta^2 - 1)$, (see Fig.2).

Expressions for \dot{W}'_k and \dot{W}'_d are given by (9) and (10), and the functions g_1 and g_2 for the assumed velocity field are

$$g_1(\alpha, \eta) = \frac{\eta^2}{(\eta^2-1)^2} \left\{ \frac{1}{16\alpha^2} \left[\frac{8\eta^2(\eta^2-\frac{1}{2})}{\eta^2-1} \ln(\eta) + 3-5\eta^2 \right] + \frac{1}{3} \right\} \quad (21)$$

$$g_2(\alpha, \eta) = \frac{\eta^2}{\eta^2-1} \left\{ \frac{\alpha}{3} + \frac{x}{R(\eta^2-1)} + \frac{1}{4\alpha} \left[\frac{2\eta^2 \ln(\eta)}{\eta^2-1} - 1 \right] \right\} \quad (22)$$

Minimization of the sum of the dissipation rate terms \dot{W}'_T , (14a), is performed at each increment of penetration Δx with respect to the parameters that describe the plastic zone, α and η . A workable procedure is to formally minimize \dot{W}'_T with respect to α which leads to a cubic in α with coefficients that are functions of η and $S_n(\dot{\epsilon})$. A numerical search technique is then employed to find values of α and η that would satisfy the minimization conditions.

Stage 2 - Bulge Formation

Once the front of the plastic zone developed in stage 1 reaches the rear free surface of the target plate, $x + \alpha R = H$ for $x = x_0$, the mode of plastic deformation transforms into one characterized by the formation of a spherical bulge on that surface. Uplifting of material at the impact surface then ceases and the material in a truncated conical sector forward of the projectile is pressed as a spherical expansion to form the bulge. This effect is clearly observed in ballistic tests, e.g. [7]. The essential physics of this mode is that of target mass movement compatible with incompressibility. The associated plastic flow velocity field determines the resisting forces acting on the projectile. No minimization procedures are therefore required for this stage.

In order to analyze the velocities and forces, it is convenient to introduce spherical coordinates, r, θ, ϕ , with origin O determined by the semi-cone angle β for the region forward of the projectile, i.e. zone II of the proposed flow field shown in Fig.3. A similar radial expansion flow field has been used by Avitzur [8] and others in analyses of metal processing. The relation between the spherical bulge geometry, and the movement of the projectile is obtained from the incompressibility requirement, namely,

$$\pi \eta_b^3 R^3 \frac{(1-\cos\beta)^2 (2+\cos\beta)}{3\sin^3\beta} = \pi R^2 (x-x_0) \quad (23)$$

where $\eta_b R$ is the radial extent of the bulge in the plane of the rear surface of the plate, and $x-x_0$ is the displacement of the projectile from the end of stage 1 (Fig.3). A further geometrical relationship can be obtained between η_b and β from Fig.3,

$$\eta_b = [(H-x)/R] (\tan\beta) + 1 \quad (24)$$

which, combined with (23), leads to an equation relating β to $(x-x_0)$,

$$\left[\frac{(H-x)}{R} (\tan\beta) + 1 \right]^3 - \frac{3(\sin^3\beta)(x-x_0)}{R(1-\cos\beta)^2(2+\cos\beta)} = 0 \quad (25)$$

This equation can be solved numerically for β for a given projectile displacement x . The bulge height in the axial direction, H_b , can also be obtained from the geometry,

$$H_b = (\eta_b R / \sin\beta) (1-\cos\beta) \quad (26)$$

In zone II, the only non-zero velocity is v_r in the radial direction r ,

$$v_r = v(r_1/r)^2 \cos\theta \quad (27)$$

where v is the projectile velocity and r and r_1 are indicated in Fig.3. For this velocity field, the strain rate components, from (1), are

$$\dot{\epsilon}_{rr} = -2v(r_1^2/r^3) \cos\theta \quad (28)$$

$$\dot{\epsilon}_{\theta\theta} = \dot{\epsilon}_{\phi\phi} = v(r_1^2/r^3) \cos\theta \quad (29)$$

$$\dot{\epsilon}_{r\theta} = -(1/2)v(r_1^2/r^3) \sin\theta \quad (30)$$

Based on the velocities and strain rates in zone II, the work rates \dot{W}_v , \dot{W}_d and \dot{W}_k could be calculated for that zone as they were obtained in stage 1 using eqs.(3,4,7,8).

Zone I is considered to be a "dead" zone with the material moving uniformly with the projectile velocity v so that a tangential velocity discontinuity exists on the interface between zones I and II. The shear work rate $\dot{W}_s^{(12)}$ due to the velocity jump across the boundary between zones I and II is calculated from eq.(5). Zone I also contributes a work rate \dot{W}_d but not \dot{W}_k and \dot{W}_v since the velocity is constant throughout that volume.

Zone VI is unaffected by the flow process. The boundary of III, IV and V, $\eta_0 R$, is the value for ηR obtained at the end of stage 1, when $x=x_0$. The velocity field for zone V is not specified since its influence on the stage 2 process would be negligible except, possibly, for frictional forces acting along the projectile surface. The work rate

of the frictional forces \dot{W}_f is again calculated by the methods described for stage 1. Zone IV is a narrow region at the rear surface and its contributions are negligible.

A proper velocity field for zone III of Fig.3 would be difficult to construct. Instead, the overall influence of this region is considered in an approximate manner. From observations of cavity cross-sections, e.g. [7, 9], it is seen that this region acts primarily as a transition zone which undergoes shearing deformation due to the material velocity along the interface with zone II (assuming no discontinuity in that velocity) and the absence of material movement in zone VI.

The shear strain rate in zone III, $\dot{\gamma}_3$, is assumed to be constant along a circular arc $d(r')$, Fig.3, and is approximated as the velocity at the interface with zone II, v_{23} , divided by the radial width of the zone described by the arc length d so that

$$\dot{\gamma}_3 = (R^2 v \cot \beta) / [(r')^2 \beta (\eta_0 R - r' \sin \beta)] \quad (31)$$

where r' is measured from the origin O along the interface surface A_{23} . On the basis that the plastic work rate in the zone III volume is due entirely to shearing deformation, the term $\dot{W}_V^{(3)}$ can be expressed by eq.(3) where $\dot{\epsilon}_3^{eff} = (\dot{\gamma}_3)_{avg} / \sqrt{3}$. The average shear strain rate in zone III can be calculated by integrating (31) over the volume of zone III and dividing by the volume V_3 .

Since the detailed velocity field of zone III is not specified, the work rates due to the dynamic effects, \dot{W}_d and \dot{W}_k , are approximated by the work rate of equivalent body forces (per unit volume) acting on the target material in zone III. Those body forces are assumed to be proportional to $\dot{\gamma}_3$ as an approximation to both the local and convective acceleration effects. The coefficient of proportionality, K_b , is obtained by enforcing continuity of the total resisting force acting on the projectile at the time corresponding to the transition from stage 1 to 2. Although K_b has the dimension of dynamic viscosity, it is not a material property but a parameter that represents overall inertial resistance to flow in an approximate manner. In the absence of other information, K_b is taken to be constant throughout stage 2 and the subsequent stage 3. The inertial work rate term for zone III is therefore approximated as

$$\dot{W}_I^{(3)} \cong \int_V (K_b \dot{\gamma}_3) \dot{\gamma}_3 dV \quad (32)$$

In actual computations for relatively thick target plates, the contribution of (32) is small compared to that for $\dot{W}_V^{(3)}$ so the approximate nature of (32) is not significant.

The total work rates for stage 2 would therefore consist of the dynamic term from zone I, the shear term from the interface of zones I and II, the various terms from zone II, the shearing and inertial terms for zone III, and the frictional term from zone V. These would then be used in the energy balance equation (13) to obtain the motion and

forces at each increment of projectile displacement. For this stage, the velocity field is completely specified by the requirements of incompressibility and geometry so that the determination of parameters by a minimization procedure is not required. Stage 2 continues until $x=x_b$ when the bulge width $\eta_b R$ reaches a maximum value, $\eta_b^{\circ} R$. Further continuation of the deformation mode would lead to physically unrealistic situations which indicates that another deformation mechanism initiates at that condition.

Stage 3 - Bulge Advancement

Guided by observations of bulge formation and growth, e.g. [7,9] the alteration to the deformation pattern is taken to be an axial displacement of the bulge region with the new bulge radius $\eta_b R$ ending on the former bulge surface, Fig.4. This bulge advancement is due to target material displaced by the projectile, and the resulting geometry is determined by the incompressibility condition.

From Fig.4, an increment of projectile displacement Δx leads to an advance in the bulge where the new spherical increment has a sector angle β and the coordinates of its intersection with the former bulge surface are $\eta_b R$ and ξ . The relation between the geometrical parameters is

$$\frac{(1-\cos\beta)^2 (2+\cos\beta)}{\sin^3\beta} - \frac{(1-\cos\alpha)^2 (2+\cos\alpha)}{\sin^3\alpha} - \frac{3\Delta x}{\eta_b^3 R} = 0 \quad (34)$$

where α is the radial angle from the former sector origin O^- to the new boundary limit $\eta_b R$, and is given by

$$\alpha = \sin^{-1} [(\eta_b / \eta_b^-) \sin\beta^-] \quad (35)$$

and η_b^- and β^- are geometrical parameters from the previous step. The other necessary geometrical relations are

$$\beta = \tan^{-1} [R(\eta_b^- - 1) / (H + \xi - x)] \quad (36)$$

$$\xi = \xi^- + (\eta_b^- R / \sin \beta^-) (\cos \alpha - \cos \beta^-) \quad (37)$$

and the current bulge height H_b is given by

$$H_b = \xi + (\eta_b R / \sin \beta) (1 - \cos \beta) \quad (38)$$

These equations are sufficient for obtaining the bulge geometry at each increment of projectile displacement. The work rates of the various forces associated with the plastic flow field could be calculated by the procedures described for stage 2 and these stages will be fully continuous. Stage 3 of bulge advancement could continue even for $x > H$.

Failure Mechanisms

The penetration processes described by stages 1 to 3 are common to a large range of ballistic impact conditions, but the terminal stage leading to failure of the target and exit of the projectile is characterized by a number of possible mechanisms. Some of these are described and illustrated in [9]. It is possible for stages 2 or 3 to lead directly to a terminal stage. This could occur by the development of adiabatic shear bands on the interface A_{23} of zones II and III, (Figs.3,4) or to the target material being relatively brittle and failing in shear on that surface. Such early failures in the penetration process lead to separation of a truncated conical sector (a conical plug) consisting of zones I and II, (Figs.3,4) from the target plate and are "low energy" modes of plugging failure as discussed, e.g. in [10].

Alternatively, and more commonly for ductile targets that do not fail by adiabatic shearing, a conventional plugging mechanism of "intermediate" energy (with a cylindrical plug) could develop from stages 2 or 3 by the formation of a flow field with a shear zone within the maximum bulge radius. For this mode, the radius of the ejected plug is essentially equal to or less than that of the projectile.

Very ductile target plates, which exhibit "high energy" ballistic resistance could experience failure by mechanical instability of the system when stage 3 is carried out to its geometrical limitation. The resulting plug is relatively short and has a spherical cap which is the frontal part of

the bulge. This and the preceding modes of failure are described in more detail in the following sections. They are the ones most commonly observed in ballistic tests on metallic plates, but other failure mechanisms and combinations of the above modes are also possible.

a. Adiabatic Shearing

The appearance of adiabatic shear bands on surface $A_{2,3}$ during stages 2 or 3 would lead to a velocity discontinuity (slip) along $A_{2,3}$ (Figs.3,4) thereby separating the interior of zone III from the resisting force field. A physical description of the process is given in [10], and an analytical treatment of the formation of adiabatic shear bands in metals subjected to rapid shear deformations is presented in [11]. It is possible to modify the calculations for stages 2 and 3 for this condition so that a flow field analysis leading to failure can be obtained. In this analysis, the plastic and inertial work rates of zone III are neglected and a shear work rate on $A_{2,3}$ is considered. From (5) and (6), this term is

$$\dot{W}_S^{(2,3)} = (2\ell n\eta_b)/(\sqrt{3}\tan\beta) \quad (39)$$

Shear strains would accumulate in the band region during stage 3 and an approximate measure of the shear strain at the rear surface is $\gamma \approx \xi/[R(\eta_b^0 - \eta_b)]$. Failure will occur at $x = x_s$ when $\gamma = \gamma_{cr}$ where $\gamma_{cr} \approx \sqrt{3}\epsilon_{cr}$. The mass of the ejected target material (plug) consists of zones I and II, Fig.4, at the failure condition and its average velocity

could be obtained by momentum considerations from the velocity field. Initially, the projectile and plug will move together but they will separate as the projectile is slowed due to frictional forces.

b. Brittle Failure in Shear

Shear failure along the interface A_{23} could take place when the material rupture condition is reached along that surface during stages 2 or 3. There is no velocity discontinuity along A_{23} prior to failure by this mode so the standard methods for stages 2 and 3 are used and an appropriate rate dependent failure criterion is introduced which involves integrating $(\dot{\gamma}_3)_{avg}$ over the time. Upon the critical condition being realized, a truncated conical plug will eject as in the previous case.

c. Plug Formation and Exit (Stages 4 and 5)

Conventional plug formation could commence at any time during stages 2 and 3 and has to be examined in parallel with the bulging processes. The mode having the lower resistance to continued penetration will be the active one. Plugging could occur in a variety of geometries and could also combine with scabbing to form complex failure modes as indicated by Fig.3e of [9]. A complete analysis would require consideration of each geometry but only the simple cylindrical plug is described in this section.

The flow field assumed for plug formation (stage 4) is shown in Fig.5 alongside the field for stage 3. For this mode,

all the target material in zone I forward of the projectile is assumed to move at the projectile velocity v and is restrained by shear stresses in zone II. Zone III is considered to contain fractured material and to be ineffective in shear. The coordinate ζ defining the boundary between zones II and III is obtained by setting the shear strain at that point due to the prior shear deformation in stage 3, approximated by $\zeta/[R(\eta_o-1)]$, equal to the ultimate strain γ_{cr} . Those zones are assumed to be limited in width to the maximum bulge diameter $\eta_b^o R$ on the basis of physical observations so that the shear strain rate along the interface of the plug and the restraining zone is

$$\dot{\gamma}_2 \approx v/[R(\eta_b^o-1)] \quad (41)$$

If transition to plugging occurs during stage 2, then the current value of the bulge width, $\eta_b R$ is used instead of $\eta_b^o R$ in (41).

Once the plugging mode has formed, further projectile advancement is resisted by the work rates of the inertial forces of zones I, II and III, the shear work rate in zone II, and by friction along the lateral surface of the projectile. These quantities are determined in a manner similar to those of stages 2 and 3. In calculating the work rates of the inertial forces in zones II and III (Fig.5) the parameter that represents dynamic effects in stages 2 and 3, K_b [eq.(32)], must be modified to account for the difference in the velocity field. A similarity argument is used to obtain a new value of

K_p for this stage.

The plug length H_p is obtained from the geometry,

$$H_p = R(\cot\phi - \cot\beta_p) \quad (42)$$

where
$$\phi = \sin^{-1}(\sin\beta_p/\eta_b) \quad (43)$$

and β_p is the sector angle for the flow field of stage 2 or 3 at the onset of plug formation, $x = x_p$.

The bulge will continue to advance until the ultimate shear strain is realized in zone II. At this condition, $x = x_s$ where $x_s = x_p + H_e$ and $H_e = \gamma_{cr} R(\eta_b^0 - 1)$. The plug will then detach and exit with the projectile. A distinct exit stage (stage 5) can be considered consisting of the projectile subjected to frictional forces, and a free cylindrical plug with a cap corresponding to the bulge shape.

d. Ductile Failure

If failure by any of the previously described or alternative modes does not occur, then stage 3 would continue until a mechanical instability condition is reached. This arises when the projectile displacement beyond the rear surface of the target exceeds the bulge advancement coordinate ξ leading to high shear stresses on the surface A_{23} , Fig.4. It is reasonable to expect that failure would then precipitate on A_{23} and that a plug will form consisting of zones I and II at that condition ($x > H$) which will have a spherical cap slightly

wider than the projectile. This capped plug would stay attached to the projectile as it exits from the plate and will subsequently separate.

Numerical Examples

Numerical exercises based on variations of the ductile plugging exit mode were carried out for the cases of A.P. projectiles of 7.62 mm diameter reported in [7] and [12]. Ductile plugging was observed in those tests to be the dominant exit mechanism and was accompanied in a few instances by scabbing and fragmentation. Only the hard core of the A.P. projectile was considered for the calculations. The core was idealized to be a rigid cylindrical rod having the maximum core diameter of 6.1 mm and the actual core length of 23.8 mm. The strain rate parameter in (2) was taken to be $C = 0.025$ based on tensile test results, and the friction coefficients were set to be $\mu_f = 0.10$ and $\mu_l = 0.05$. A value of $\mu = 0.10$ is given in the literature for dynamic metal working conditions and a lower value should be used here for the lateral surfaces because of the higher velocities and temperatures.

The computed and test results are listed in Table 2, from which it appears that the predictive capability of the present analysis is fairly good. Some further explanations are required for reading Table 2. All the test results listed are given in [12] and those of tests 1, 2, 3 are also presented in [7]. For some reason, the value of b for test 3 in [7] is not consistent with the correct value given in [12] and in Table 2. The width of the shear zone in the tests, e , was measured to be the maximum extent of the visible

shear strains, e.g. Figs. 5, 7 of [7], and the corresponding quantity in the present analysis is $R(n_0-1)$ listed in the last column of Table 2. Examination of cavity cross-sections, e.g. Figs. 5, 7 of [7], were used to obtain b , the length of the shear zone within the original target thickness. The corresponding parameter in the analysis is $H-x_0$ where x_0 is the extent of the penetration at the end of stage 1. Predicted plug lengths, H_p , obtained from the computations for stage 4 are listed, but test data for the actual plug lengths is not available. As expected, $H_p < (H-x_0)$ in this analysis whereas b is assumed in [1] to correspond to the plug length.

Test results for the final velocity of the projectile give a range of values which are a consequence of the ejected plug and fragments activating the measurement system prior to the projectile in some of the tests. Calculated values for the final projectile velocity based on the present analysis are generally within the experimental range and appear to be more consistent with the test results than those of [1,7]. Predicted plug velocities are slightly higher than those of the projectile because of the friction on its lateral surface during stage 5.

In addition to the primary exit modes discussed previously, there are secondary differences in the exit mechanisms. A number of possible variations of the basic ductile plugging mode have been incorporated in the calculation procedure and the one appropriate for the test was used. It is recognized

that this procedure is an empirical input and corresponds, in effect, to distinguishing fine differences in the exit behavior. These differences appear to be related to the observed scatter of terminal velocity values for nominally identical test conditions which is especially pronounced near the ballistic limit. The variations of the ductile plugging mode that were considered are as follows:

- P_0 - a fully ogival shaped plug within the cylindrical boundary.
- P_1 - a cylindrical plug with an ogival nose, e.g. Fig. 3b of [9].
- P_2 - a fully cylindrical plug as described in stage 4 of the analysis, e.g. Figs. 4, 8 of [7], Fig. 3a of [9].
- P_3 - a cylindrical plug with a wider head (combined plugging and scabbing) due to the combination of zones I and III in stage 4 (Fig. 5), e.g. Fig 3e of [9].

Two plugging conditions were calculated for test 7 since the actual shape seemed to have features of both P_1 and P_2 . The results are an example of the range in final velocity values obtainable from variations in the basic plugging mode.

Calculated histories of the projectile displacement, velocity, and resisting force are shown in Figs. 6 and 7 for tests 2 and 3. For the thinner target, test 2 - Fig. 6, the duration of the high resisting force during stage 1 is very short, 1.6 μ s, and stages 2 and 3 play an important role. A rapid drop in the resisting force occurs during stage 4 (at

$t = 10.3 \mu\text{s}$, $x = 7.4 \text{ mm}$) due to separation of the assumed cylindrical plug (P_2) from the target plate at that instant. Stage 4 continues until the plug is fully ejected from the target plate. The maximum value of x , 33.4 mm, is the distance for complete exit of the projectile from the deformed target at the end of stage 5. Calculated items not listed in Table 2 for test 2 are: plug mass 0.6 g, maximum bulge height 3.7 mm, maximum bulge diameter 10.1 mm. Effective strain rates in the bulge region and along the surface A_{23} of stages 2 and 3 were of the order of 10^5 sec^{-1} . Test 3, Fig. 7, was for a thicker target plate and the duration of stage 1 is longer, 8.5 μs . Again, stages 2 and 3 are important factors. Plug separation takes place at $t = 22.1 \mu\text{s}$ when $x = 13.7 \text{ mm}$ but, because of the assumed ogival plug shape (P_0), there is no sharp drop in the resisting force during stage 4. Additional computed quantities for this case are: plug mass 0.5 g, maximum bulge height 3.8 mm, maximum bulge diameter 10.5 mm. Effective strain rates were about 1/3 lower for the thicker target plate.

Acknowledgements

The authors would like to thank Mr. Michael Barak for his expert assistance with the computational work and Mrs. Denise Meiselles for her diligent typing of the manuscript.

REFERENCES

- [1] J. AWERBUCH and S. R. BODNER, Int. J. Solids Structures 10, 671 (1974).
- [2] A. TATE, Int. J. Engng. Sci. 17, 341 (1979).
- [3] J. B. MARTIN, Int. J. Solids Structures 8, 1185 (1972).
- [4] J. TIROSH and S. KOBAYASHI, ASME J. Appl. Mech. 43, 314 (1976).
- [5] U. S. LINDHOLM, J. Mech. Phys. Solids 12, 317 (1964).
- [6] D. IDDAN and Y. TIROSH, "Upper Bound of Deep Indentation" ASME Journal of Engineering for Industry 99B, 804 (1977).
- [7] J. AWERBUCH and S. R. BODNER, Int. J. Solids Structures 10, 685 (1974).
- [8] B. AVITZUR, E. D. BISHOP and W. C. HAHN, Jr., "Impact Extrusion - Upper Bound Analysis of the Early Stage", ASME Journal of Engineering for Industry 94B, 1079 (1972).
- [9] M. A. BACKMAN and W. GOLDSMITH, Int. J. Engng. Sci. 16, 1 (1978).
- [10] G. B. OLSON, J. F. MESSALL and M. AZRIN, in Shock Waves and High Strain-Rate Phenomena in Metals (Edited by M. A. Meyers and L. E. Murr), Plenum Pub. Corp., New York, 221-247 (1981).
- [11] A. M. MERZER, J. Mech. Phys. Solids 30, (1982).
- [12] J. AWERBUCH, "Experimental and Analytical Investigation on the Mechanism of Projectile Perforation in Metallic Plates", D.Sc. thesis, Technion, Haifa, Israel (1972).

Zone Notation	Velocity Field: v_i			Strain Rate Field: $\dot{\epsilon}_{ij}$			
	v_r	v_θ	v_z	$\dot{\epsilon}_{rr}$	$\dot{\epsilon}_{\theta\theta}$	$\dot{\epsilon}_{zz}$	$\dot{\epsilon}_{ij}$ for $i \neq j$
I	$\frac{vR}{2\alpha R}$	0	$-\frac{vz}{\alpha R}$	$\frac{v}{2\alpha R}$	$\frac{v}{2\alpha R}$	$-\frac{v}{\alpha R}$	0
II	$\frac{v(\eta^2 R^2 - r^2)}{2\alpha R r (\eta^2 - 1)}$	0	$\frac{vz}{\alpha R (\eta^2 - 1)}$	$-\frac{v(\eta^2 R^2 + r^2)}{2\alpha R r^2 (\eta^2 - 1)}$	$\frac{v(\eta^2 R^2 - r^2)}{2\alpha R r^2 (\eta^2 - 1)}$	$\frac{v}{\alpha R (\eta^2 - 1)}$	0
III	0	0	$\frac{-v}{\eta^2 - 1}$	0	0	0	0
IV	0	0	0	0	0	0	0

Table 1 - Particle Velocities and Strain Rates for Each Zone of the Plastic Flow Field Assumed During Stage 1 of the Penetration Process

Test No.	Steel Alloy Target Description			Experimental Results and Measurements						Analytical Predictions*				
	Thickness H (mm)	Yield Stress (quasi-static) σ_0 (kg/mm ²)	Strain to Failure ϵ_{cr} (%)	Shear Zone Length b (mm)	Width of Shear Zone e (mm)	Striking Velocity V_s (m/sec)	Final Velocity V_f (m/sec)	Exit Mode*	3 Stage [†]			Current (5 Stage)		
									Final Velocity V_f (m/sec)	Final Velocity V_p (m/sec)	Plug Length H_p (mm)	Final Velocity V_f (m/sec)	Plug Length H_p (mm)	Width of Shear Zone "e" $R(r_0-l)$ (mm)
1	6.0	98	20	5.0	-	835	550-650	P_3	499	660	677	3.9	5.4	4.6
2	6.35	120	20	5.0	-	848	500-600	P_2	492	589	621	3.3	5.0	4.5
3	12.0	90	20	5.5	5.5	855	300-390	P_0	418	364	424	3.4	5.6	6.0
4	8.0	98	10	7.0	4.5	852	630-680	P_3	-	640	661	4.3	5.4	5.0
5	8.0	80	20	6.0	-	842	600-650	P_0	-	608	633	5.2	5.8	5.3
6	8.1	130	20	5.6	4.5	847	350-450	P_1	-	401	468	3.1	4.9	4.7
7	9.0	90	20	7.5	5.0	849	590	$\left. \begin{matrix} P_1 \\ P_2 \end{matrix} \right\}$	-	521	559	3.7	5.7	5.3
8	10.0	90	20	8.5	3.8	835	450-500	P_1	-	453	499	3.6	5.6	5.5

Table 2 - Analytical Predictions and Test Results from [7] and [12].

*See section on "Numerical Examples"
[†]From References 1 and 7

Caption for Figures

- Fig. 1 - Schematic of five stage sequence of deformation mechanisms for perforation process.
- Fig. 2 - Plastic flow field for stage 1 of perforation process - dynamic plastic deformation.
- Fig. 3 - Plastic flow field for stage 2 of perforation process - bulge formation.
- Fig. 4 - Plastic flow field for stage 3 of perforation process - bulge advancement.
- Fig. 5 - Plastic flow field for stage 4 of perforation process - plug formation.
- Fig. 6 - Predicted histories of projectile displacement, velocity, and resisting force during perforation process (Test No.2, Table 2).
- Fig. 7 - Predicted histories of projectile displacement, velocity, and resisting force during perforation process (Test No.3, Table 2).

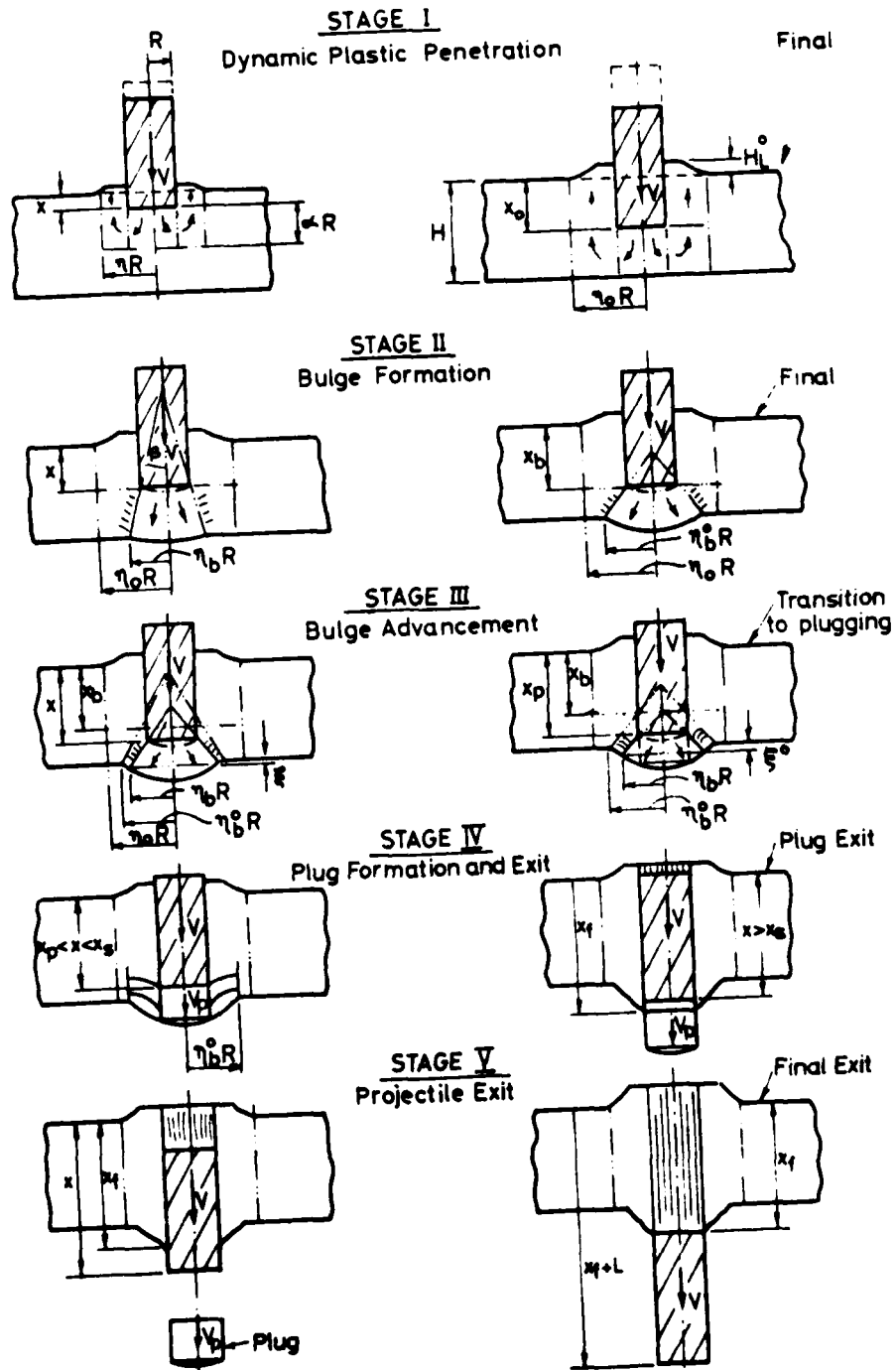


FIG. 1

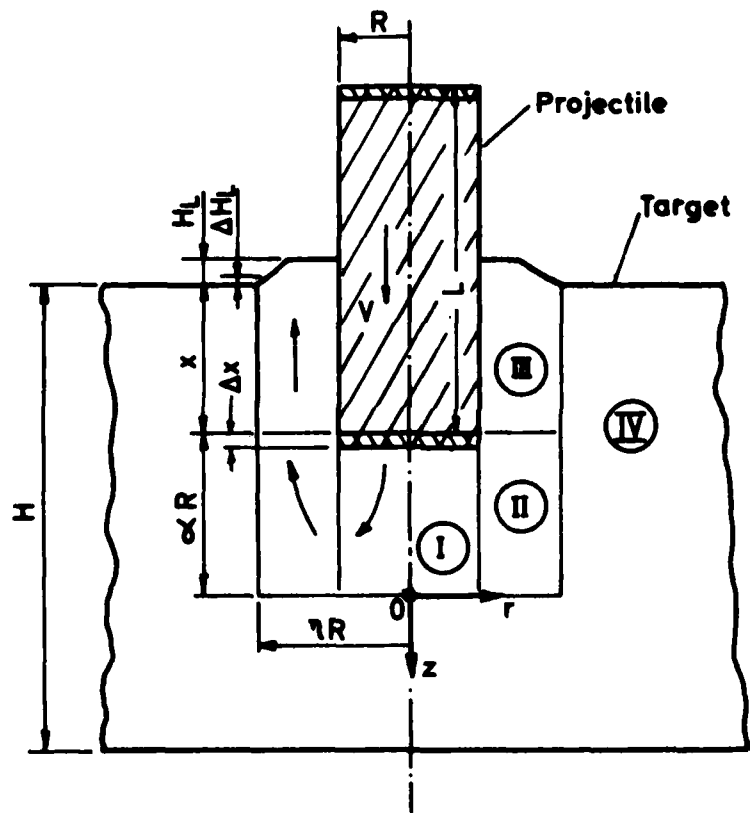


FIG. 2

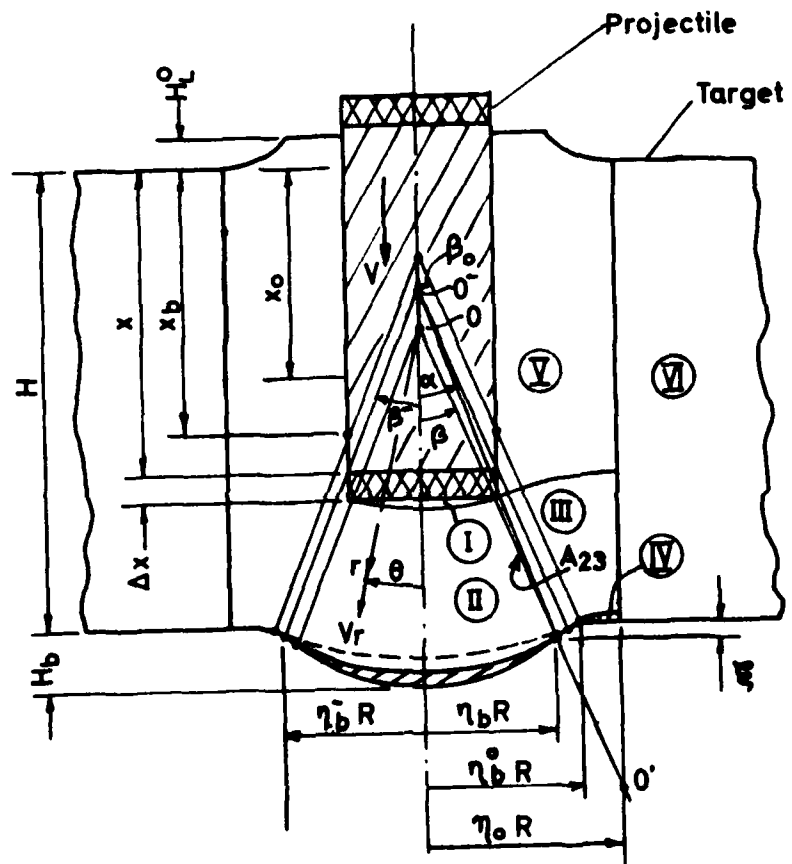


FIG. 4

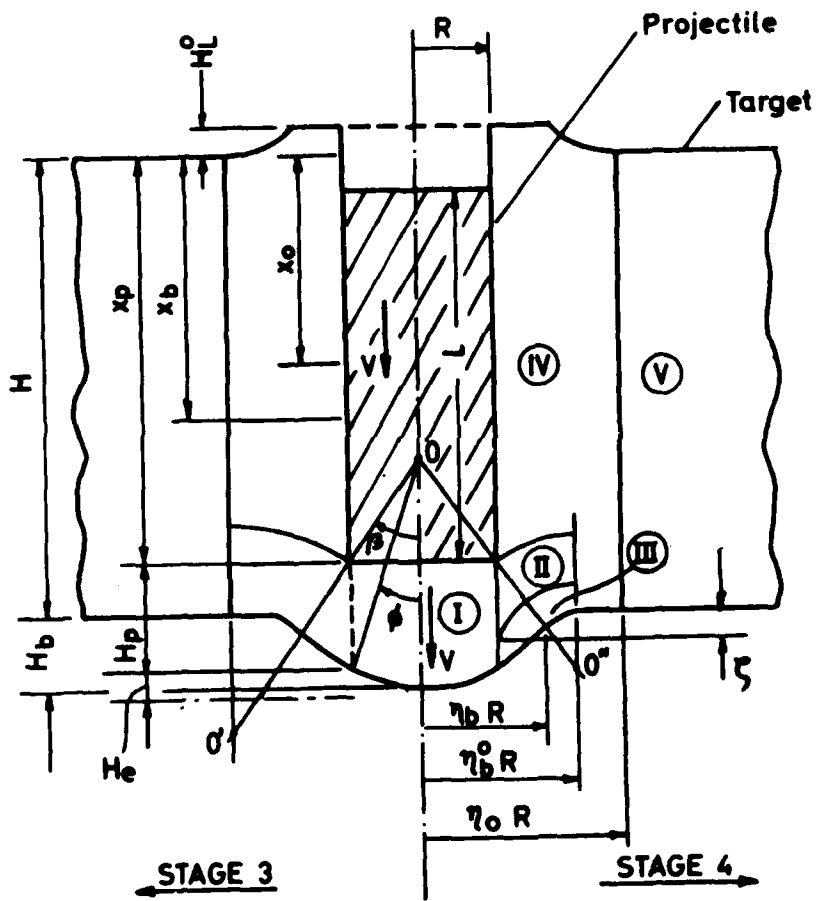


FIG. 5

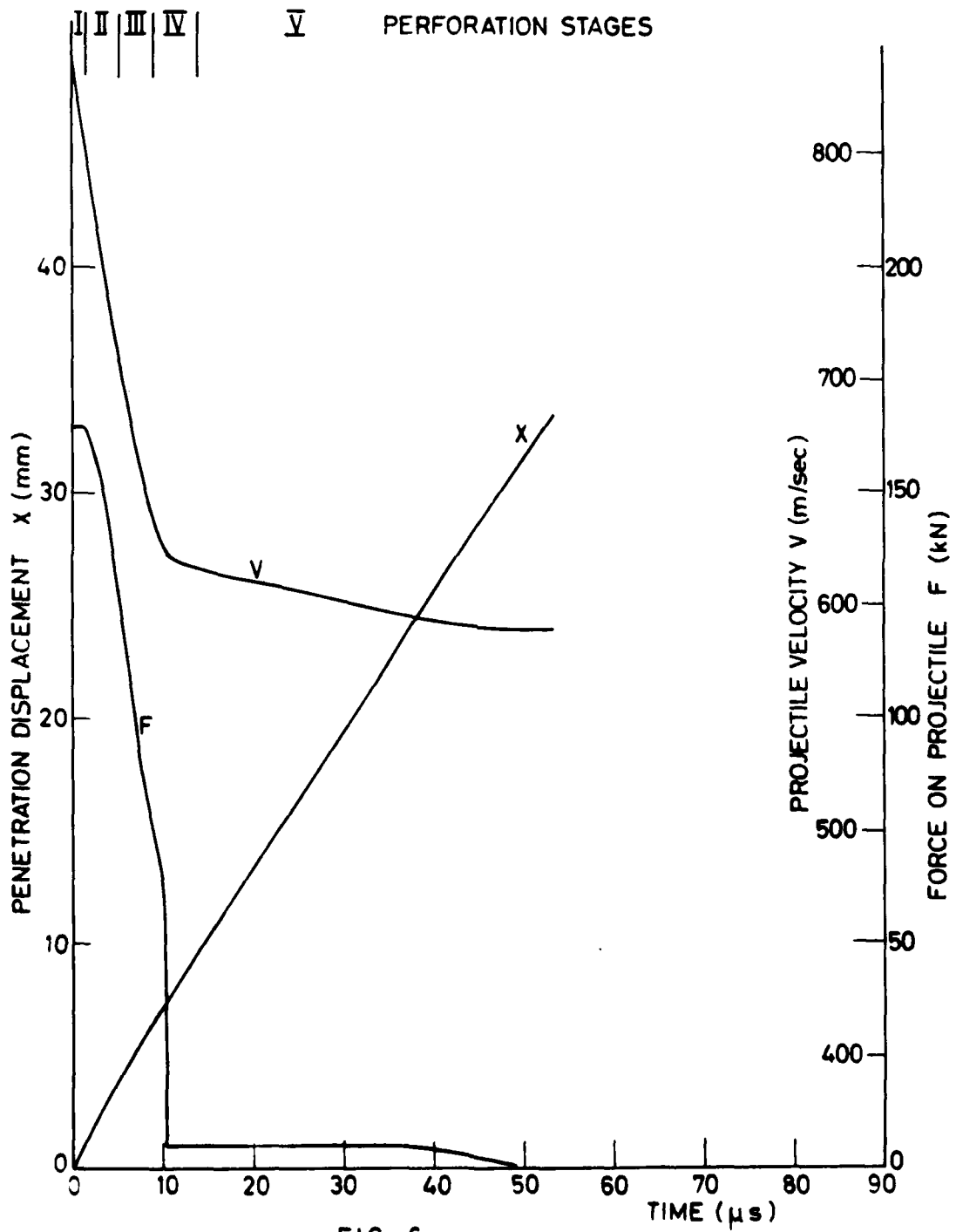


FIG. 6

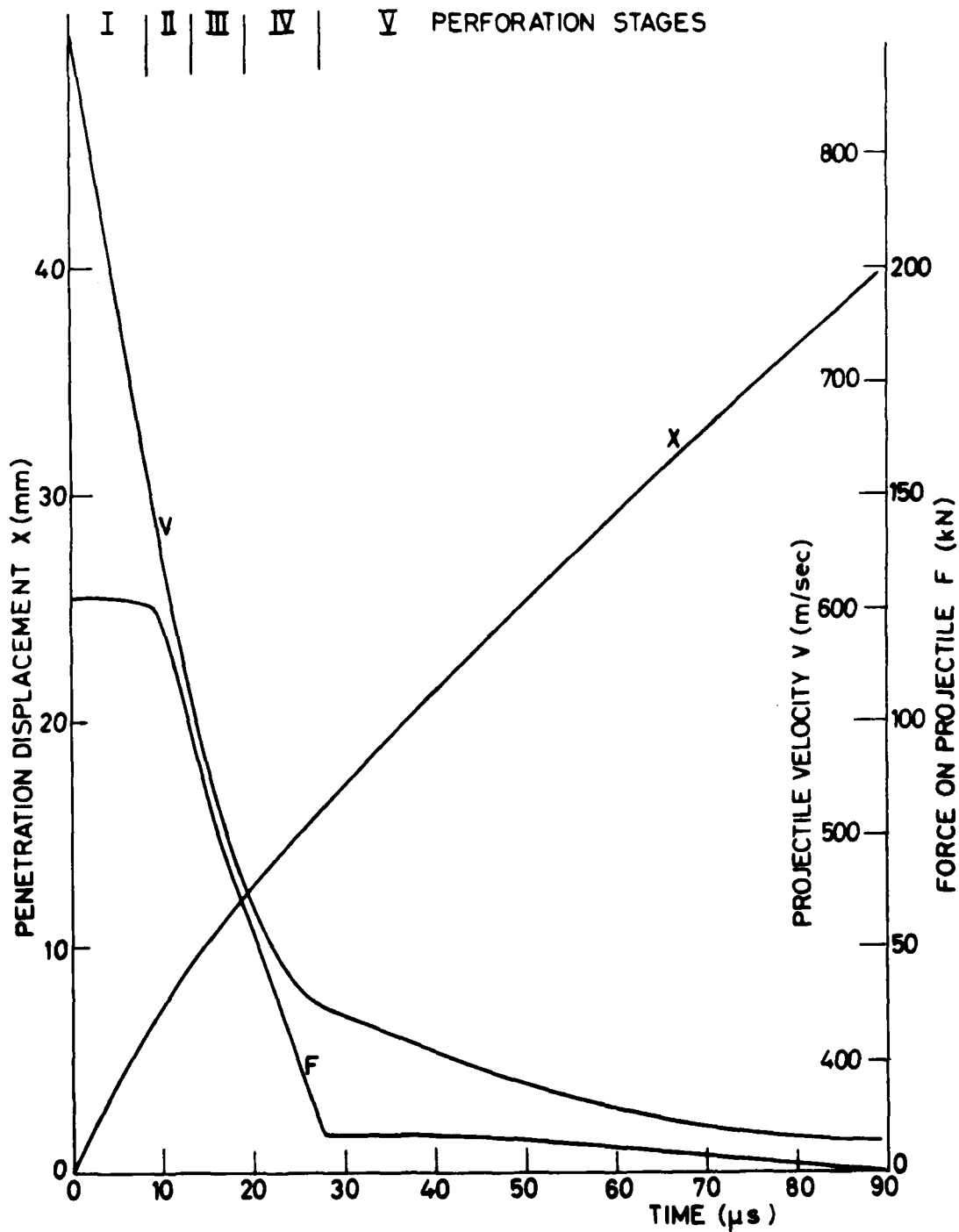


FIG. 7